Colloids and Surfaces A: Physicochemical and Engineering Aspects 713 (2025) 136513

Contents lists available at ScienceDirect

Colloids and Surfaces A: Physicochemical and Engineering Aspects

journal homepage: www.elsevier.com/locate/colsurfa

A novel freezing-sublimation-based method for enhancing deposition uniformity of colloidal particles in inkjet 3D printing: A proof-of-concept study

Haipeng Zhang, Xiaoxiao Zhang, Yang Liu *

Department of Mechanical Engineering, The City College of New York, New York, NY 10031, United States

GRAPHICAL ABSTRACT

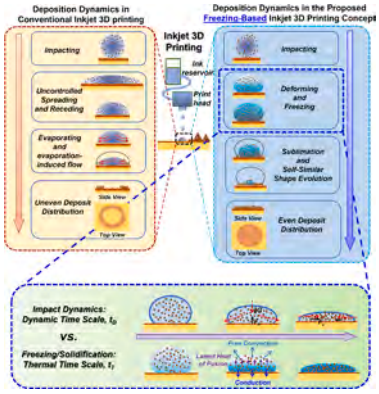

ARTICLE INFO

Keywords:
Droplet impingement
Droplet spreading
Freezing
Sublimation
Particle deposition

ABSTRACT

Inkjet-based three-dimensional (3D) printing is widely used for fast and efficient non-contact manufacturing, yet it suffers from several drawbacks, such as coarse resolution, lack of adhesion, manufacturing inconsistency, and uncertain final part mechanical properties. These undesirable effects are related to complex flow phenomena in colloidal droplets in inkjet 3D printing, particularly the internal flows and droplet deformations during the deposition and drying processes. These challenges are due to the colloidal suspension droplets being kept in the liquid state during printing. To overcome these disadvantages, this paper presents a novel freezing-sublimation-based inkjet 3D printing concept that freezes the colloidal droplets upon impact followed by sublimation, eliminating the undesirable particle transport and fluid motions during deposition. A series of experiments were conducted to characterize the colloidal droplet behaviors during the impinging/freezing and sublimation processes and evaluate the effects of the freezing process on droplet impinging dynamics as well as the final deposition patterns through sublimation. It was demonstrated that the deposition patterns obtained from this new method are much more uniform than the conventional evaporation-based deposition method. Both qualitative and quantitative methods were applied to analyze the colloidal droplet profiles during the printing process (impinging, freezing, and sublimation), as well as the final deposition patterns. The study shows promising

* Corresponding author.
E-mail address: yliu7@ccny.cuny.edu (Y. Liu).

https://doi.org/10.1016/j.colsurfa.2025.136513
Received 4 December 2024; Received in revised form 6 February 2025; Accepted 24 February 2025
Available online 25 February 2025

results of using this new method, providing a foundation for the development of the novel freezing-sublimation-based inkjet 3D printing technique.

Nomenclature

μ	Viscosity of droplet
ρ	Density of droplet
ρ_p	Density of colloidal particles
ρ_{air}	Density of air
σ	Surface tension coefficient of droplet in air
θ	Static contact angle of droplet on the substrate
AR	Area ratio of the printed pattern on the substrate
Bi	Biot number
Bo	Bond number
c	Specific heat capacity of droplet
D	Droplet diameter on the substrate
D_d	Initial droplet diameter
D_p	Diameter of colloidal particles
D_{max}	Maximum spreading diameter of droplet on the substrate
g	Gravitational acceleration
H	Height of droplet on the substrate
h	Convective heat transfer coefficient of droplet
h_d	Equivalent thickness of droplet at its maximum spreading diameter
H_{sl}	Latent heat of ice
I	Intensity of colloidal particles on the substrate
I_{max}	Maximum intensity on the substrate
I_{min}	Minimum intensity on the substrate
k	Thermal conductivity of droplet
L	Characteristic length of droplet
m	Mass of droplet
N_d	The number of pixels in the expected deposition area on the substrate
N_p	The number of pixels in the printed area on the substrate
R	Radius of the printed pattern on the substrate
R_T	Thermal resistance of droplet
Re	Reynolds number
S_{max}	Maximum spreading ratio of droplet
St	Stokes number
t	Time
t_0	Initial time point
T_d	Temperature of droplet
T_F	Freezing temperature of droplet
T_s	Surface temperature of the substrate
$t_{freezing}$	Freezing time of droplet
V	Impact velocity
We	Weber number

1. Introduction

Three-dimensional (3D) printing is an additive manufacturing (AM) process that has received much attention in recent decades. Compared to the traditional subtractive manufacturing methods, 3D printing has brought in new design freedom and economic advantages, making it a perfect fit for custom designs and prototype fabrications [1–3]. Many 3D printing methods have been developed, including stereolithography (SLA), selective laser sintering (SLS) or melting (SLM), fused deposition modeling (FDM), direct energy deposition (DED), and inkjet-based 3D printing, favoring the different manufacturing needs while being applicable to a variety of materials [2–4]. Among these technologies, inkjet-based 3D printing is recognized as a competent tool for manufacturing complex and advanced structures of various materials, with growing demands from aerospace, healthcare, biomedical, and automotive industries [1,4].

Conventional inkjet-based 3D printing methods create 3D structures layer-by-layer by jetting colloidal suspension droplets onto a substrate with subsequent evaporation and deposition [1,2,5]. Usually, there are two modes of inkjet printing: continuous mode and drop-on-demand mode. In both of these two inkjet mechanisms, liquid colloidal drops are jetted through an orifice or nozzle. Continuous printing can produce drop jetting with generation rates in the range of 20–60 kHz and velocities of more than 10 m/s [6]. While this offers fast processing, it is more vulnerable to contamination as the ink is recycled [1]. The drop-on-demand printing mode generates individual colloidal drops at acoustic frequencies of 1–20 kHz and velocities of 5–8 m/s [7]. This method has higher resolution and is considered more economical. However, the drying of ink at the nozzle during downtime may cause clogging and further jetting errors [1]. In general, the ink liquid properties, such as viscosity, surface tension, and density, must be within certain ranges to allow inkjet printing to work correctly. The performance of inkjet-based 3D printing is generally evaluated in terms of drop placement accuracy, resolution, manufacturing consistency, and final part mechanical properties [8], which are determined by the colloidal droplet dynamics during jetting, impacting, spreading, and drying processes [4,5].

One big challenge in inkjet 3D printing is the coarse printing resolution, which is essentially determined by the droplet-substrate interactions in the printing process, i.e., droplet impact, deposition, and the subsequent drying processes. The droplet impinging dynamics on solid surfaces have been extensively studied [9]. Various dynamic phenomena have been observed, including splashing, spreading, receding, and bouncing. For a colloidal droplet impacting a solid substrate, the drop would spread to a maximum due to the dissipation of the kinetic energy of the droplet. After the spreading stage, the drop recoils back to an equilibrium shape that is determined by the surface energies of the liquid and the solid surface. The dynamics of an impacting droplet is significantly affected by liquid drop properties (i.e., viscosity, surface tension, density, velocity, and diameter) and surface conditions (i.e., roughness, wettability, and shear modulus) [9–12]. As a result, the resolution of inkjet-based 3D printing (i.e., printing drop footprint) would essentially depend on the ink drop volume, drop spreading cap size, and contact angle between drop and substrate.

During the evaporation-based drying processes of colloidal droplets, various solid deposit patterns could form due to free surface movement, contact line dynamics, and diverse internal flow structures that may present during the evaporation processes [13–15]. The so-called coffee ring pattern has been commonly observed, which forms due to the radial capillary outward flow inside the sessile drop that replenishes the faster drying at the rim of the drop [16]. Meanwhile, the surface tension gradient along the drop radial direction generated from the vapor pressure difference contributes to the Marangoni flow that can reverse the replenishing flow and produce different deposit patterns [14]. Contact line dynamics also play an important role in determining the evaporation rate, the internal flow structures, and particle transport behaviors during the drop evaporation process [17]. Since the inkjet droplets may have different sizes and surface energies, the viscous and inertial forces of the droplets vary significantly during the printing

process. Moreover, the substrate surface properties and ambient conditions (*e.g.*, humidity) also strongly affect the depositing dynamics during the droplet evaporation [18]. As a result, the drying mechanism and hence the final deposit pattern can be substantially different during the various inkjet 3D printing processes. This has been the main source of course resolution, defect formation, and manufacturing inconsistency in inkjet-based 3D printing technologies.

When a colloidal droplet evaporates with a pinned contact line, the coffee ring effect may occur due to the outward capillary flow that carries the solute particles to the edge of the evaporating droplet [16]. This effect can be suppressed by either weakening the outward capillary flow or increasing the inward Marangoni flow [19]. The outward capillary flow can be suppressed by raising the ambient humidity, reducing the droplet size, or introducing responsive droplets with corresponding applied external fields [19,20]. The inward Marangoni flow is produced when the surface tension gradient presents along the radial direction of a droplet [21]. This flow carries the particles near the substrate surface to the top of the droplet [14] and can be enhanced by adding surfactants [20,22]. Attempts to produce desired deposition morphology also include jetting colloidal droplets on specifically patterned substrates [19] to adjust spreading and wetting behaviors. For example, the use of a hydrophilic-hydrophobic surface pattern can generate desired deposit patterns and improve the printing resolution and accuracy [23]. To control the deposition morphology in inkjet-based 3D printing and improve the printing resolution and manufacturing consistency, various strategies have been developed, including tuning the liquid properties [22,24,25], regulating ambient conditions [26], employing surface patterning [18,27], applying external fields [19], modulating the pH of the ink droplet by utilizing supporting water droplets [28], precisely adjusting the drying and overlapping processes of neighboring ink droplets during printing [29], and operating the printing process on porous cellulose nanopaper surfaces [30].

Despite the noticeable advances made in controlling deposition morphology in inkjet-based 3D printing, their applicability is highly limited due to the very complex and variable solute particle behaviors and solvent motions in different colloidal droplets that evaporate from different substrate conditions. This has been the bottleneck preventing inkjet-based 3D printing from becoming a more widespread AM technology. In this paper, as the first effort of its kind, a novel freezing-sublimation-based method is developed to prevent the uncontrolled transport of particles in colloidal droplets during the drying process in 3D printing. This method fundamentally enhances the deposition uniformity of colloidal particles during printing, which can be adopted across various inkjet-based printing applications. Different from the conventional evaporation method to deposit and form solid structures from liquid suspensions, this freezing-sublimation-based approach can essentially eliminate the undesired drop spreading, fluid motions, and solute transport behaviors during manufacturing processes. While many freezing-based methods have been developed and implemented in 3D printing in the past decade [31–34], these methods have mainly focused on packing solute particles between growing solvent crystals to form desired networks and porous structures through sublimation of the solvent. In these methods, the freezing-sublimation process is applied as a specialized treatment to the entire 3D-printed part, creating the desired internal porous structures.

In this paper, however, the use of freezing-sublimation is not to produce network structures, but to offer more precise controls of drop spreading and deposition uniformity in much broader inkjet 3D printing applications beyond the existing freezing techniques of fabricating porous structures. In this method, the ink droplets are instantly frozen upon contact with the substrate, after which the frozen solvent is removed through a sublimation process. With well-controlled pressure, humidity, and temperature conditions during freezing and sublimation, the undesired overspreading, particle transport, and fluid motions can be eliminated.

To demonstrate this novel concept, a series of experiments were conducted in this study to evaluate both the dynamic and thermal processes during the droplet impacting and freezing processes. In addition, the final deposition patterns formed through freezing and sublimation were also captured and analyzed. In the context that follows, the theoretical background of both the evaporation-based and freezing-sublimation-based inkjet printing processes are first introduced. Then, the experimental methods to study the droplet behaviors during impacting, freezing and sublimation processes are described. Both high-speed imaging and infrared thermal imaging techniques were utilized to characterize the evolutionary details of the droplet during the freezing-sublimation-based printing process. A series of image processing methods are also introduced, followed by an in-depth discussion of the measurement results of the droplet dynamics and thermal evolutions during impacting and freezing, as well as the final deposition patterns.

2. Theoretical background

Conventional inkjet-based 3D printing involves multiple stages, including droplet impingement and subsequent drying. In practical applications, the ink droplets typically have diameters in the order of micrometers [35,36]. This small scale makes it particularly challenging to accurately characterize the droplets' transient hydrodynamic behavior and heat transfer properties during the printing process. To more intuitively replicate and elucidate the behavior of colloidal droplets and the resulting particle distribution patterns on substrates in our proposed method, this proof-of-concept study employed millimeter-scale droplets. Although discrepancies may arise in this large-scale laboratory model system, a detailed scaling analysis of the experimental data (in the following sections) indicate that many underlying physical processes are shared across scales, which is the focus of this paper.

Fig. 1 shows time sequence images of printing a colloidal droplet (0.5 % (w/v) Pearlitol 100 SD solution) on a hydrophilic substrate at room temperature. Fig. 1(a) ~ (e) illustrates the hydrodynamics of the droplet during the impinging process on the substrate (t_0 indicates the initial contact). Right after the initial contact, the droplet spread to its maximum diameter (D_{max}) and then retracted and stabilized in a static state. Under experimental conditions with a low droplet impact velocity (V), no break-up splash or rebounding from the surface was observed. Instead, the droplet only deformed on the surface during impingement, called the deposition regime [37]. After the droplet stabilized in its static state, the contact line of the droplet was pinned on the substrate. As shown in Fig. 1(f) ~ (j), the droplet evaporated over time with a constant contact area. In the end, colloidal particles remained on the substrate, forming a coffee-ring-like pattern. Very few colloidal particles was seen at the center of this printed pattern.

The transient diameter (D) and the height (H) of the droplet on the substrate during these dynamic processes were measured to quantify the geometrical shape change of the droplet over time (t). Fig. 2 shows the temporal variations of the normalized D and H of the droplet during impingement and evaporation-based drying processes on the substrate at room temperature. Here, D indicates the horizontal distance from the left to the right boundary of the droplet on the substrate, and H shows the vertical distance between the substrate and the highest point of the droplet.

Two stages, impingement and evaporation-based drying, can be distinguished from Fig. 2 based on different trends of D and H. In the impingement process, the droplet spread and reached its maximum diameter after impacting the substrate. After that, the droplet retraction occurred. The contact line receded towards the center of the droplet till the droplet became static. This process is represented in the former part of Fig. 2 as follows: after initial contact, D increased rapidly with decreasing H. It implied that a spherical droplet was flattened on the substrate, corresponding to the spreading process of the droplet. In a short period, D achieved its maximum spreading diameter, more than three times D_d, and started the retract process immediately, during

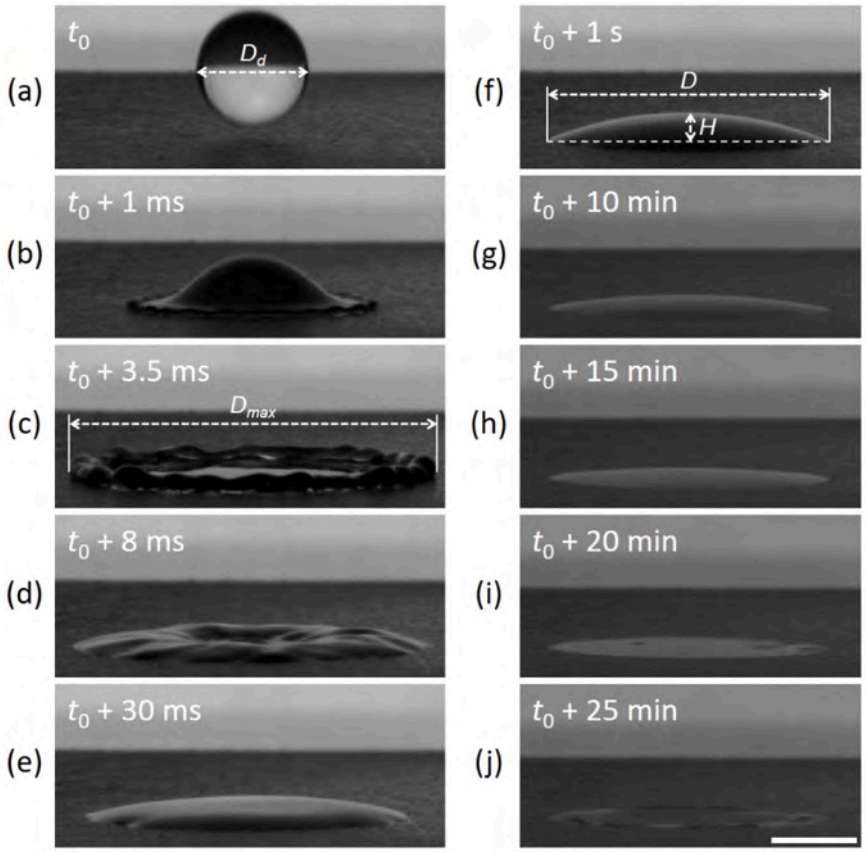

Fig. 1. The time-evolution of a colloidal droplet during the impingement process, *i.e.,* (a) ~ (e), and the evaporation-based drying processes, *i.e.,* (f) ~ (j), on a hydrophilic substrate at room temperature. $D_d = 2.70$ mm, $V = 1.92$ m/s. (Scale bar: 2 mm).

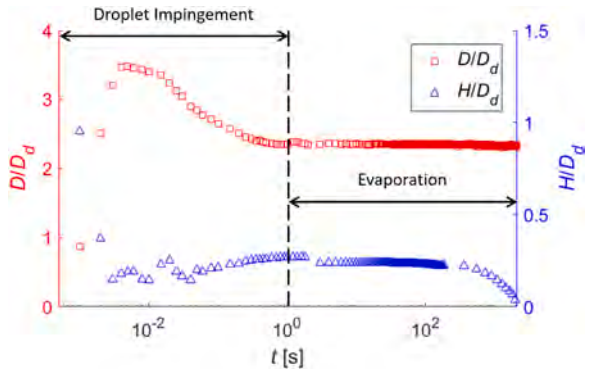

Fig. 2. A linear-log plot to show the geometrical shape change of a colloidal droplet during the impingement and evaporation-based drying processes on a hydrophilic substrate at room temperature. $D_d = 2.54$ mm, $V = 1.84$ m/s. D and H indicate the diameter and the height of the droplet on the substrate, respectively.

which D decreased with increasing H. Ultimately, the droplet displayed features of a sessile droplet on the substrate. Both D and H achieved constant values, indicating that the droplet reached a spherical cap-like shape that can well balance surface tension forces along solid-liquid, solid-air, and liquid-air interfaces acting at the contact line.

As time goes by, water molecules were released from the liquid surface into the air due to the vapor gradient at the surface, enabling evaporation-based drying. In Fig. 1, the contact area of the droplet was almost constant during evaporation, and only the height of the droplet gradually decreased. This observation was confirmed from the latter part of Fig. 2: D had a negligible change during the evaporation process with decreasing H. It suggested that the contact line of the droplet was pinned on the substrate during this process. Evaporation was fast near the contact line of the droplet, which has a high curvature of the droplet profile. It induced an internal flow from the center towards the boundary of the droplet to refill the loss of water. The induced flow can bring suspending colloidal particles to the edge of the droplet. In the end, solid particles gathered along the boundary of the droplet and formed a ring-shaped pattern on the substrate [38–40]. This internal flow is undesired as it can cause a nonuniform distribution of colloidal particles on printed patterns. To examine fluidic motions that may affect the distribution of colloid particles in inkjet-based 3D printing, theoretical models for droplet impingement and the drying process on substrates were summarized as follows.

2.1. A. Evolution of droplet impingement on substrates

When a colloidal droplet was ejected onto a substrate, the droplet deformed instantly due to the inertial effects. During the process of droplet impingement, the role of gravitational effects on the dynamic process of droplet deformation was considered in relation to the size of the droplet. The Bond number ($Bo = (\rho - \rho_{air})gL^2/\sigma$) was used to quantify the significance of the gravitational effect, which was obtained from the ratio of gravitational to capillary forces. Here, $(\rho - \rho_{air})$ indicates the density difference between the colloidal solution and air, g is the gravitational acceleration, L is the characteristic length of droplets, and σ is the surface tension coefficient. When Bo is smaller than 1, it indicates that gravitational and surface tension forces are balanced in the droplet, and the gravitational effect is not dominant in the shape of the droplet.

Besides gravitational effect, the deformation morphology varies based on the impact Weber number, which is a function of impact velocity on the substrate (V) and the physical properties of this colloidal

solution, including the density (ρ), the viscosity (μ), and the surface tension coefficient (σ). At the room temperature, if the Weber number ($We = \rho V^2 D_d/\sigma$) of droplet impact was small, and the surface wettability of the substrate was hydrophilic, the droplet would spread along the substrate without splashing or bouncing off from the surface [41–44]. During this spreading process, D would increase until the surface tension and viscous forces within the droplet overcame the inertial force of the droplet. Then, the droplet would recoil with a decreasing D. The receding contact line would also lead to a decreased contact angle of this droplet. In the end, the droplet achieved its static state when the contact angle could balance all surface tensions along interfaces well.

The maximum diameter of the droplet during spreading (D_{max}) is one of the critical parameters to characterize this spreading regime. D_{max} can be predicted using dimensionless numbers representing fluidic behaviors during droplet impingement. For instance, with a known D_d, D_{max} can be obtained from S_{max}, the spreading ratio between D_{max} and D_d (*i.e.*, $S_{max} = D_{max}/D_d$). In practice, S_{max} can be approximately calculated as follows [45]:

$$S_{max} = \sqrt{\frac{4}{3} Re^{\frac{1}{4}}} \tag{1}$$

where

$$Re = \frac{\rho V D_d}{\mu} \tag{2}$$

However, it should be noted that the droplet impinging dynamics and the associated droplet morphology and contact diameter, D, can be significantly altered when the substrate surface is at freezing temperatures. Depending on the heat transfer rate, the droplet could freeze or solidify on the substrate at any moment during contacting, spreading or retracting, inhibiting further D changes [46]. Here, the thermal process of droplets freezing on the substrate can also be affected by the size of the droplets. With this regard, the Biot number ($Bi = hL/k$) can be used to evaluate the effects of droplet size on the freezing process, where h is the convective heat transfer coefficient, L is the characteristic length of droplets, and k is the thermal conductivity of the colloidal solution. When $Bi < 0.1$, the temperature distribution within the spreading droplet is effectively uniform, indicating that the droplet is in a thermally homogenous state, and its size has a minimal effect on the freezing process [47].

2.2. B. Evolution of droplet evaporation

After impingement, the geometrical shape of a static sessile droplet on substrates was governed by surface tensions along three interfaces: solid-liquid, solid-air, and liquid-air interfaces. When these forces achieve balance, the corresponding angle between the tangential directions along air-liquid and liquid-solid interfaces is called static contact angle, which depends on the surface properties of substrates. Also, the sessile droplet would form a spherical cap-like shape to minimize its surface energy.

During evaporation, water molecules in the sessile droplet would escape from the liquid surface to become vapor at room temperature. Depending on whether or not the contact line is pinned on the substrate, the evaporation mode of the droplet varies: either the droplet has a constant contact area or a constant contact angle during evaporation. For the former mode, the droplet usually has an initial contact angle of less than 90∘ on the substrates [48]. With an almost constant contact area on the substrate, the contact angle of the droplet decreased linearly over time during the drying process [38,49]. For the latter mode, the contact line continuously recedes during evaporation, producing a more complicated process with a changing wetted area of the droplet [50]. This mode occurs more often with unique substrate surface structures and droplet deposition conditions, for instance, when the initial contact angle of the droplet is greater than 90∘ [48]. It should be noted that most studies were focused on the evaporation mode of a droplet with a constant contact area on substrates, as shown in Fig. 1, as it occupies 90 ∼ 95% of the droplet's lifetime during evaporation [51].

In addition, the geometrical shape of droplets during evaporation is predictable. Assuming that the droplet on substrates is a spherical cap, the total height of the free surface (h) of any point on the profile of a droplet on substrates can be represented as [52]:

$$h(r,t) = \sqrt{\frac{R^2(t)}{\sin^2\theta(t)} - r^2} - R(t)\cot\theta(t) \tag{3}$$

Here, r is the horizontal distance from the center of the droplet ($r = 0$), and t is the time duration since the beginning of evaporation. $R(t)$ and $\theta(t)$ are the radius and the contact angle of the droplet as a function of t, respectively. The boundary condition of this equation, $h(R) = 0$, illustrates that the contact line is pinned on the substrate. With a pinned contact line, the R of the droplet is constant over time.

It was found that the water mass decreased linearly over time. Thus, the contact angle of a droplet decreased linearly with time for a droplet with a pinned contact line on substrates. An approximation equation of the contact angle of the droplet during evaporation is obtained: $\theta(t) = \theta_i(1 - t/t_f)$. Here, θ_i is the initial contact angle of the droplet on substrates. t_f is the required total evaporation time till the free surface of the droplet became flat on substrates.

The above equations inform that the evaporation rate varies significantly at the droplet surface with a curvature. When the contact line is pinned on the substrate, most water loss occurs near the contact line of the droplet during evaporation. Hence, an internal flow is induced from the center toward the boundary of the droplet to refill the water loss at the edge [53]. This flow can redistribute the suspended colloidal particles toward the contact line region of the droplet during the evaporation process. When the droplet is completely dried, most colloidal particles would deposit near the contact line of the droplet. This phenomenon, which caused a non-uniform distribution of particles, formed a ring-like pattern on the substrate and was known as the "coffee-stain" effect [53–55].

2.3. C. Evolution of droplet sublimation

The geometrical shape of a frozen water droplet during sublimation has been well studied. It was found that both D and H of a frozen droplet would decrease, and the contact angle would not be constant during the sublimation process. A frozen droplet's sharp edges with high curvatures were observed to be rounded and smoothed rapidly at the beginning of sublimation. It is worth mentioning that the mass loss of the frozen droplet is not refillable during sublimation. In addition, sublimation that occurred by step motion could easily relocate weakly bonded frozen water molecules at the edges of the droplet to form new steps on their adjoining faces. On these formed steps, newly exposed frozen water molecules sublimated easily and formed new steps in a continuing process during sublimation, resulting in the droplet's tips and edges becoming rounded [56,57]. This smoothing process could increase the contact angle of a frozen sessile droplet to around 90∘ in a short period at the early sublimation stage.

After the smoothing process, the geometrical shape of a frozen droplet exhibits a self-similar behavior during the late stage of sublimation. An equation to express the shape change of a frozen droplet at the late time of sublimation was derived as follows [56]:

$$R(t) = \sqrt{R_0^2 - 2\beta\left(C_0^{pro}/H_0\right)t} \tag{4}$$

$$H(t) = \frac{H_0}{R_0} R(t) \tag{5}$$

The time, t, in this equation is the time duration since the beginning of the late stage of sublimation, which can be approximately determined

as $t = t_f/2$. R and H measured at $t_f/2$ were used as initial values, R_0 and H_0, of this equation.

In addition, β is an evaporation parameter calculated from $\beta = D_c(\rho_{sat} - \rho_\infty)/\rho_{ice}$, D_c is the constant diffusion coefficient. ρ_{sat}, ρ_∞, and ρ_{ice} indicate the constant saturation value of the vapor mass concentration at the ice surface, a fixed value of the vapor mass concentration far away from the ice surface, and the density of ice, respectively. C_0^{pro} indicates the initial capacitance for a prolate spheroids-shaped droplet. Here, a, b, and c are the three semi-axes of an ellipsoid droplet. With $b = c$, the capacitance can be simplified as:

$$C^{pro} = \frac{2\sqrt{a^2 - b^2}}{\ln\left(\frac{a+\sqrt{a^2-b^2}}{a-\sqrt{a^2-b^2}}\right)} \tag{6}$$

The solvent (such as water) can be removed via sublimation, but colloidal particles contained in the droplet remain, forming patterns through the mechanism of random propagating deposition of solid particles in three dimensional on the substrate after the droplet is completely sublimated [40]. It should be noted that small voids may be created during the sublimation process due to the escape of vapor from inside of the frozen droplet [58]. However, these voids would be much smaller in comparison to the voids formed due to the nonuniform deposition in the conventional evaporation-based drying process.

3. Materials and methods

3.1. A. Materials

In this study, 0.5 % (w/v) Pearlitol 100 SD solution was used as the inkjet solution. The solution was prepared by mixing the Pearlitol powder (E131G, Roquette) with distilled water. Average mean diameter and the density of the powder particle were $D_p = 100$ μm and $\rho_p = 1.514$ g/cm^3, respectively. The physical properties of this solution were measured at room temperature using electronic balance (TE32FT digital scale, Taylor), a rheometer (MCR 302, Anton Paar) with a 50 mm-diameter cone geometry (1∘), and the pendant drop method-based image analysis [59], respectively ($\rho = 1000$ kg/m^3, $\mu = 0.88$ mPa·s, and $\sigma = 57.2$ mN/m). The measured solution properties are similar to water, which implies that adding a small amount of Pearlitol powder would not affect the physical properties of water significantly.

The substrate for 3D printing was made from aluminum plates (20 mm × 20 mm × 1 mm) with surface treatments. Each plate was polished with two types of sandpapers in order (#800 and #2000 grids) and then was painted using black paint (Painter's Touch Ultra Cover 2 ×, Paint + Primer, Flat Black, Rust-Oleum). After that, the plate was placed into a fume hood overnight to allow the painting to dry. The contact angle, θ, of the inkjet solution on the substrate was measured as $\theta \approx 23$∘ based on the $\theta/2$ method from side view images captured by a high-speed camera [60].

3.2. B. Experimental setup

To study the droplet impingement and freezing, as well as the sublimation-based drying processes, a customized test rig was developed, consisting of two sections: the impinging and freezing platform and the freeze-drying chamber. Fig. 3 shows the first section that can generate droplets and release them onto substrates to produce droplet impinging and freezing processes. Colloidal droplets can be generated by injecting the prepared colloidal solution through a tubing connected to a nozzle from a syringe (10 mL plastic syringe, inner diameter = 14.5 mm, Vita Needle Company) using a syringe pump (NE-300, New Era Pump Systems, Inc.). A needle (Size 26, inner diameter = 0.26 mm, Vita Needle Company) is fixed on a homemade frame on an optical table as the nozzle. The volume flow rate of the syringe pump for colloidal solution injection was 0.1 mL/min. The distance between the needle tip and the substrate surface is adjustable, e.g., in this paper, the droplet falling distance was set to be around 180 mm.

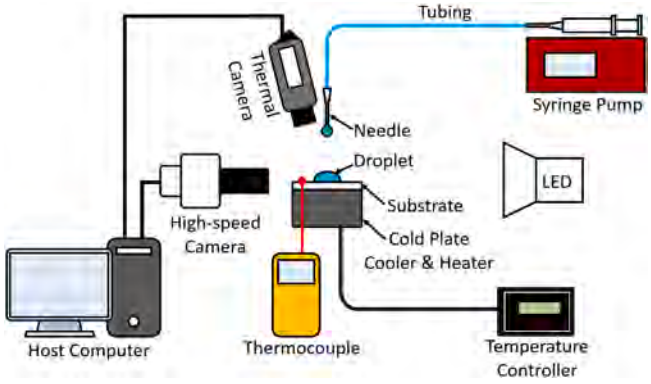

Fig. 3. A schematic of the test platform for studying droplet impingement and freezing processes on a precooled substrate.

A thermoelectric-Peltier cold plate cooler & heater (CP-061HT, TE Technology, Inc.) was fixed on the optical table as a test stage. An aluminum plate with proper surface treatment was placed on the cold plate as the substrate. The cold plate was connected to a pulse width modulated temperature controller (TC-48–20, TE Technology, Inc.) and a power supply (PS-24–6.5 A, TE Technology, Inc.) to adjust the surface temperature of the cold plate and precool the substrate. A thermocouple (DT304 Apollo IV Digital Temperature Logger, UEi Test Instruments) was connected to the substrate's surface to detect and monitor the substrate's surface temperature (T_s) in each experiment.

A high-speed camera (Phantom VEO 440-L, Vision Research) and a thermal infrared camera (FLIR A655sc, FLIR Systems AB) were mounted on the optical table to record droplet impingement on substrates from the side and the top views, respectively. For highspeed imaging, an LED light (RS-5620, RPS Studio CooLED 200 Studio Light, Dot Line Corp) was used for illumination.

Fig. 4 shows the second section of the test rig that provides a sublimation-based drying process for droplets frozen on the substrate. It includes a commercial freeze dryer (HRFDS, Harvest Right, LLC.) and a vacuum pump. After the droplet impingement and freezing processes are completed, the substrate with the frozen droplet is transported into the freeze dryer chamber for the sublimation process. Side-view images of droplet sublimation are recorded using a monochrome digital camera (DMK 23U445, The Imaging Source) through the observation window of the freeze dryer. An LED light (RS-5620, RPS Studio CooLED 200 Studio Light, Dot Line Corp) was used to provide illumination. A homemade light reflector board was used in the freeze dryer chamber to provide enough illumination for imaging purposes.

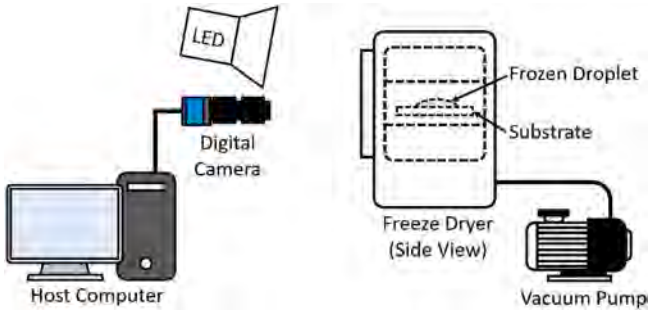

Fig. 4. A schematic of the test platform for studying the sublimation-based drying process of a droplet frozen on a substrate.

3.3. C. Experimental procedure

Fig. 5(a) illustrates the experimental procedure in this study, including dripping a colloidal droplet, freezing the droplet on a precooled substrate, and sublimating the droplet in a freeze dryer. In detail, a substrate was placed on the cold plate and precooled till $T_s \approx$ -10 ℃ for preparation. After that, a colloidal droplet was generated at the needle tip above the substrate by pumping the colloidal solution from a syringe using a syringe pump. A low volume flow rate (= 0.1 mL/min) was applied to minimize the inertia effect on the droplet. With a continuous injection process, the suspending droplet kept growing, and eventually, the droplet pinched off from the needle tip and impinged on the substrate. In this study, the droplet size was determined by the size of the needle (inner diameter = 0.26 mm for size 26 needle), measured as D_d = 2.54 ~ 2.70 mm. The impinging velocity of droplet, V, is determined by the distance from release to impact (accelerated due to gravity), e.g., V = 1.82 ~ 1.92 m/s in this study.

Upon impacting the precooled substrate, the droplet would rapidly freeze on the surface. A high-speed camera and a thermal infrared camera were simultaneously triggered to record this process, from the droplet's initial contact with the substrate to its static state on the substrate due to freezing. After that, the substrate with the frozen droplet was transported into the freeze dryer for sublimation. An ice pack was used during transportation to prevent any possible melting of the droplet, and the sublimation chamber was precooled a lower-than freezing temperature. Then, a monochrome camera was triggered to record the evolution of the droplet. After that, the following steps were made to achieve droplet sublimation: freezing, vacuum freezing, and heating. In the beginning, the temperature inside of the sublimation chamber (T) was reduced to around −30 ℃. Then, vacuum freezing was enabled by running a vacuum pump to reduce the pressure (P) to around 110 Pa while the temperature was maintained at −30 ℃ in the chamber. After that, the heating process was launched to increase the temperature of the chamber to around 15 ℃, through which the sublimation was accomplished.

The phase change of the colloidal droplet during these processes was summarized in Fig. 5(b). When the droplet was generated at room temperature (≈ 25 ℃) at ambient pressure (101325 Pa), it was liquid. After impingement, the temperature of the droplet was rapidly reduced to below the freezing point on the precooled substrate. The droplet froze and was kept at around −10 ℃, the same temperature as T_s. This corresponds to the freezing process shown in Fig. 5(b). After that, the frozen droplet was transported into the precooled sublimation chamber without phase change. Then, the sublimation chamber was operated to decrease the pressure to 110 Pa, and then increase the temperature of the chamber to 15 ℃. Both the pressure and the temperature were lower than at the solid/liquid/vapor triple point of water (611.66 Pa and 0.01 ℃) [61], so the phase change of the droplet from solid to gas took place in the sublimation chamber. This is shown as the sublimation process in Fig. 5(b); no internal flow was induced in the droplet during the entire drying process.

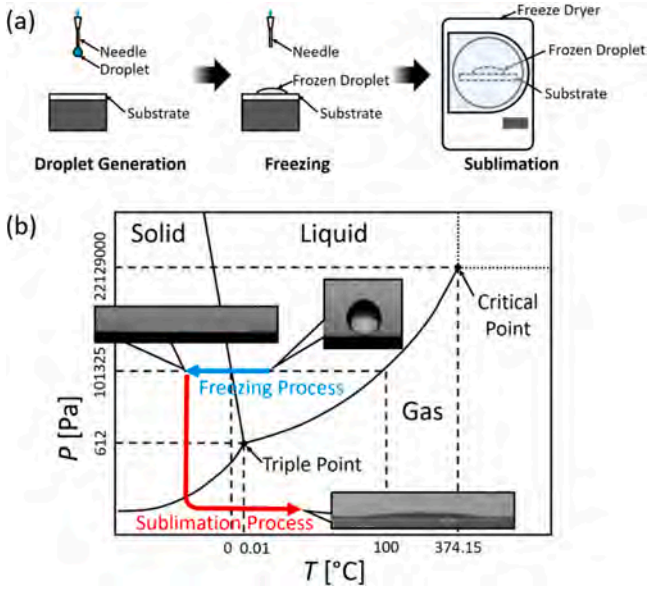

Fig. 5. (a) The experimental procedure of investigating the freezing-sublimation-based 3D printing method. (b) A schematic diagram of the phase change of a colloidal droplet during the impingement and the sublimation processes.

After the sublimation process was completed, only colloidal particles remained on the substrate. Images of the obtained printing pattern formed by particles were captured from the top using a digital camera (EOS 6D Mark II, Canon) for advanced analysis. For comparison, additional experiments were repeated using droplets without a rapid freezing process on substrates. Droplets were dripped on substrates with $T_s \approx$ 25 ℃. After the droplet's shape was static after impingement, the droplet was either left on the substrate for evaporation at room temperature or transported with the substrate into the freeze dryer for sublimation. For the former case, the droplet's evolution was continuously recorded until the water phase was evaporated entirely. For the latter case, the freezing process of the droplet was done in the freeze dryer. Thus, as mentioned previously, around one hour of freezing at −30 ℃ was required before the vacuum freezing process. Experiments were repeated multiple times to confirm the repeatability of observations (N = 1 for droplets with an evaporation-based drying process and N = 3 for droplets with a sublimation-based drying process).

3.4. D. Image processing and data analysis

3.4.1. D.1. Measurements of D_d and V of a droplet before impact

To characterize the droplet impingement condition, i.e., D_d and V, a suit of customized Matlab codes was developed to process the snapshots of droplets captured using the high-speed imaging system by following the procedures shown in Fig. 6.

At the beginning, a snapshot of the droplet before impact, as shown in Fig. 6(a), was converted into a binary image, as shown in Fig. 6(b), using Matlab's 'imbinarize' function. The 'ForegroundPolarity' parameter was set as 'dark' to indicate that the boundary of the droplet was darker than the background of the image, and the 'Sensitivity' parameter was set as '0.40'. After that, the boundary of the droplet was detected by using the 'bwtraceboundary' function. The white line shown in Fig. 6(c) indicates the detected edge of the droplet from this image. In the end, based on the detected boundary, a circular fitting was performed. The fitting result is shown in red in Fig. 6(d), in which the dotted line and the cross marker indicate the boundary and the center, respectively. D_d was obtainable from the diameter of the fitting circle. V was calculated from the average travel distance of the circle's center and the time interval over frames by repeating the same image processing procedure to other frames from the same video.

3.4.2. D.2. Measurements of D and H of a sessile droplet on substrates

The change in the geometrical shape of a sessile droplet on substrates was quantified by D and H, respectively. The procedure of image processing is summarized in Fig. 7. To begin with, a raw snapshot of the sessile droplet, as shown in Fig. 7(a), was converted into a binary image, as shown in Fig. 7(b), by the 'imbinarize' function. The 'ForegroundPolarity' parameter was set as 'bright', and the 'Sensitivity' parameter was set as '0.20'. Then, the "interfaces" were detected by using the 'bwtraceboundary' function. Then, the substrate surface boundary was detected, as marked in red in Fig. 7(c). After that, the droplet profile was probed as shown in Fig. 7(d) and (e). Thus, the critical points were obtained from the boundary to characterize the geometrical shape of the droplet, as shown in Fig. 7(f). It should be noted

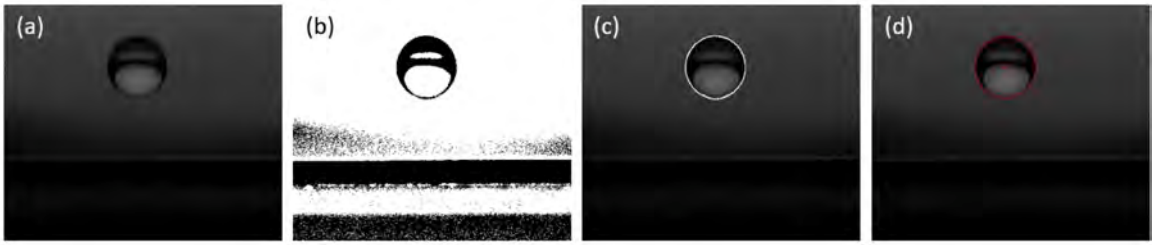

Fig. 6. The procedure of image processing to measure D_d and V from captured images of droplets before impingement. (a) Read a single frame of the droplet image from the video. (b) Convert the image into a binary image. (c) Detect the boundary of the droplet on the image. (d) Perform circular fitting using detected boundary to determine the droplet's diameter and center on the image.

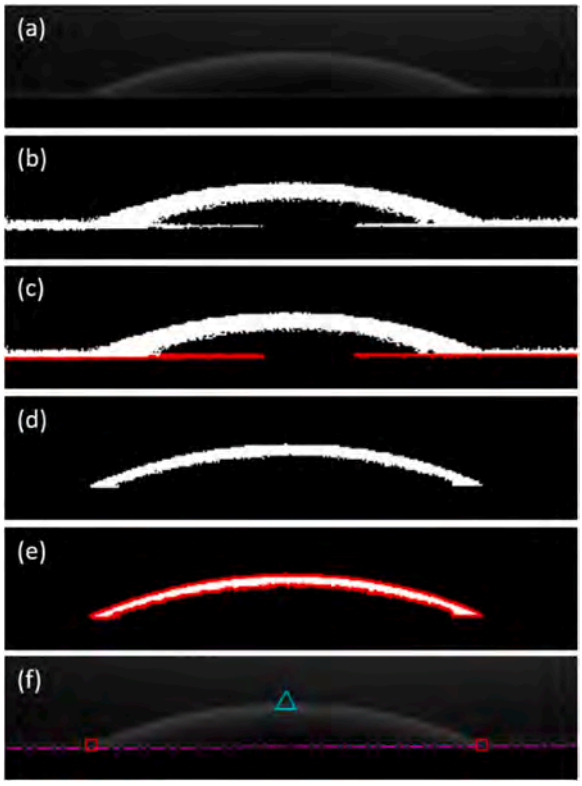

Fig. 7. The procedure of image processing to measure the evolution of D and H from images of sessile droplets on substrates. (a) Raw snapshot of a sessile droplet. (b) Convert the image into a binary image. (c) Detect the boundary of the substrate surface. (d) Binary image of the droplet profile. (e) Detect the boundary of the droplet using (d). (f) Measure D and H by referring to critical points on the droplet profile. Red square markers, the cyan triangle marker, and the magenta dash-dotted line indicating the left- and right-most points on the boundary of the droplet, the top-most point on the boundary of the droplet, and the surface of the substrate, respectively.

that, a "thick" boundary was observed in the image processing, which was caused by light reflection at the interface. The droplet boundary was defined as the outer edge of the detected object. Comparisons between the detected droplet profiles and the raw images demonstrated excellent agreement, confirming the accuracy and reliability of the image processing approach. The left-most and the right-most points on the boundary were marked as red squares, and the top-most point on the boundary was marked as a cyan triangle, respectively. The linear distance between two red square markers was measured as D. The linear distance between the cyan triangle marker and the magenta dash-dotted line, which indicates the fitting line of the substrate surface, was calculated as H. By repeating the same procedure for images extracted from multiple frames, the evolution of D and H during the drying process of droplets can be quantified.

The above procedure was applied to the droplet images captured during the sublimation process. The profile of the droplet and the location of the substrate surface were separated from the detected boundaries, respectively. In the end, D was measured from the left-most to the right-most points on the droplet profile, and H was calculated from the surface of the substrate to the top-most point on the droplet profile.

3.4.3. D.3. Characterization of deposition profiles of dried colloidal droplets on substrates

After the drying process, colloidal particles remained on the substrates and formed printed patterns. The image intensity profiles of the captured patterns were used as a reference to evaluate the printing quality.

The procedure of image processing is summarized in Fig. 8. Firstly, a raw image of the printed pattern shown in Fig. 8(a) was converted into a binary image, as shown in Fig. 8(b). Circular fitting was operated to determine the smallest circle that can enclose the entire pattern shown in Fig. 8(b). The fitting result was shown in Fig. 8(c), in a red dotted line and a red cross marker indicating the boundary and the center of the fitting circle, respectively. Then, the intensity profiles along the radius direction can be obtained, as shown in Fig. 8(d). As a reference, blue dashed lines were drawn from the center to 80 pixels away from the boundary of the circle, with both ends marked by red cross and red circle markers (10∘ apart between lines, with 36 lines in total). The intensity profiles along all these dashed lines were extracted.

As an example, the intensity profile along the 3 o'clock direction was read from an image by the 'improfile' function. The measurement result was plotted by black square markers in Fig. 8(e), where the x-axis and y-axis indicated the distance of the measured point from the center (R) and I, respectively. A linear interpolation was implemented to unify the number of extracted points along all directions, after which, new points were obtained, marked by red dots in Fig. 8(f). In the end, I values were re-scaled based on the maximum (I_{max}) and minimum intensities (I_{min}), respectively. R was normalized using D_d, too. Fig. 8(g) shows the final result, in which the x-axis and y-axis indicate R/D_d and $(I - I_{min})/(I_{max} - I_{min})$, respectively.

By repeating the same procedure, the intensity profiles along all directions were measured from the raw images. Thus, an angular-averaged intensity profile can be obtained and used to characterize the deposition patterns of colloidal particles on the substrate.

4. Results and discussions

4.1. A. Impacting and spreading dynamics of colloidal droplets on substrates with different temperatures

The effects of substrate temperature (particularly sub-freezing temperature) on the impacting and spreading dynamics of droplets were experimentally studied based on the high-speed images of droplet impingement. Firstly, the process of droplet impingement on the

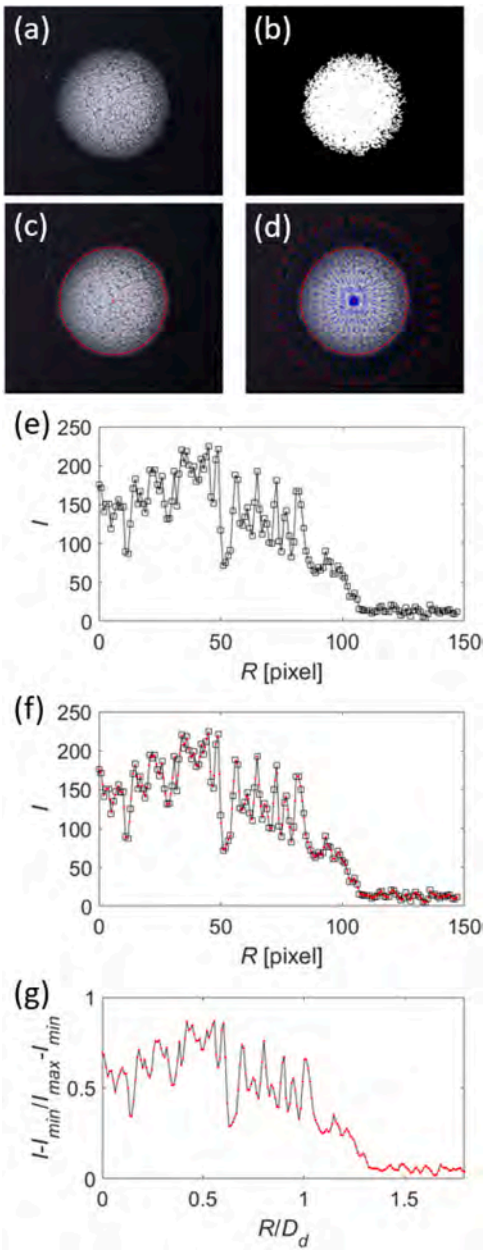

Fig. 8. The procedure of image processing to characterize the deposition patterns of colloidal droplets on substrates. (a) Read a raw image of the deposition pattern of a colloidal droplet on the substrate. (b) Convert the image to a binary image. (c) Operate circular fitting to find a minimum circle shown as a red dotted line that can enclose all deposits into a circular range. (d) Find the center of the fitting circle shown as a red cross marker. Determine the outermost points (shown as red circle markers) at 80 pixels from the boundary of the fitting circle. Connect the center of the circle with these points with blue dashed lines to indicate the location of intensity measurement. (e) Measure I of each pixel along the blue dashed line in the 3 o'clock direction. Plot measured I over R using black square markers. (f) Operate linear interpolation to obtain 200 I values from points with the same intervals of R from (e), and plot these I values using red dot markers. (g) Re-scale I and R, and plot the result using red dot markers. The x- and y-axis indicate normalized data as R/D_d and $(I - I_{min})/(I_{max} - I_{min})$, respectively.

substrate at $T_s \approx 25$ ℃ was captured, as shown in Fig. 9(a). A droplet was generated at the needle tip by injecting colloidal solutions using a syringe pump. The initial droplet diameter before impact was $D_d = 2.54$ mm, and the speed of the droplet was $V = 1.84$ m/s upon impacting on the substrate. Under these conditions, the *We* of the

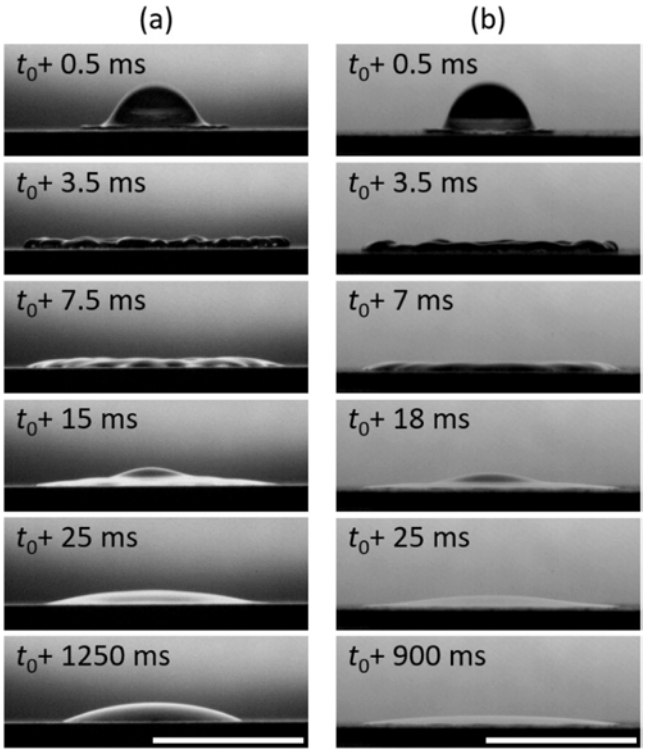

Fig. 9. The time sequence of side view images of droplet impingement on hydrophilic substrates. t_0 indicates the initial time point when the droplet contacted the substrate. (a) $D_d = 2.54$ mm, $V = 1.84$ m/s, $T_s \approx 25$ ℃. (b) $D_d = 2.58$ mm, $V = 1.84$ m/s, $T_s \approx$ -10 ℃. (Scale bar: 5 mm).

droplet was calculated to be 150.

After impinging on the surface, the droplet experienced a series of dynamic stages. Firstly, the droplet started spreading in the radial direction on the surface. A rim-lamella shape was formed during this process, including a thin central lamella part and a thick surrounding rim, which agrees with those discussed in [62] when the *We* was larger than 13.4. Additionally, the surrounding rim was wavy, caused by circumferential instability of the droplet rim. Under the low *We* condition, the inertial force is insufficient to cause a splash or breakup of the droplet [63]. The droplet was kept in direct contact with the substrate during the spreading process, which was named the deposition regime. The droplet achieved its maximum spreading diameter ($D_{max} = 8.89$ mm) at $t = 0.004$ s. After that, the droplet started to retract. The contact line started to recede towards the center of the droplet. When the contact line arrived at its equilibrium location, the contact line was pinned on the substrate. During the retraction process, the oscillation motion of the droplet continued. In the final state, the droplet became static with a spherical cap-like shape. In this shape, the contact angle of the droplet is known as the static contact angle. It could support well-balanced forces between surface tension forces along all interfaces. No significant change on the outer boundary of the droplet was observed even during the following evaporation process.

With the same substrate and experimental setup, a colloidal droplet was dripped on a precooled substrate with $T_s \approx$ -10 ℃. The droplet impacting and spreading processes are shown in Fig. 9(b). $D_d = 2.58$ mm, $V = 1.84$ m/s, and *We* of the droplet was calculated as 153 for this experiment. Since T_s was lower than the freezing temperature of the colloidal droplet, a rapid freezing of the droplet was expected. However, according to Fig. 9(b), the geometrical evolution of the droplet during the initial impacting and spreading processes was identical to that in the $T_s \approx 25$ ℃ case. After initial contact, the droplet spread in the radial direction to form a rim-lamella shape till its maximum spreading on the surface of the substrate. It suggested that the

freezing process was slower than the dynamic spreading process, i.e., the droplet remained unfrozen during the spreading stage. The geometrical evolution of the droplet during the spreading process could still be predicted based on *We*.

The retraction process of the droplets showed significant differences on the substrate under the freezing T_s condition. After the spreading stage, the contact line of the droplet was immediately pinned on the surface of the substrate. The boundary of the droplet did not recede from the maximum spreading diameter, although the colloidal droplet was not completely frozen. The colloidal solution's oscillation motion continued until the droplet became static. It suggested that a thin layer of colloidal solution at the bottom of the droplet was frozen on the substrate, inhibiting the mobility of the contact line. Although the liquid phase of the droplet above the frozen layer continued the oscillation, the outer boundary of the droplet was fixed near the maximum spreading diameter. Finally, the droplet became static and formed a thin disc-like shape, with a larger D than the spherical cap-like droplet obtained in the $T_s \approx 25$ ℃ case. It was also seen that the angle between the frozen droplet and the substrate surface was smaller than θ of the liquid-state droplet at $T_s \approx 25$ ℃.

Fig. 10(a) shows the infrared thermal images of the droplet during the impingement process on the substrate at $T_s \approx 25$ ℃. The retraction process of the droplet occurred rapidly from D_{max} on the substrate after impingement, as indicated by the dashed line in the first image of the time sequence images. During the early stage, it was seen that temperature of the droplet was around 22 ℃, which was slightly lower than T_s,

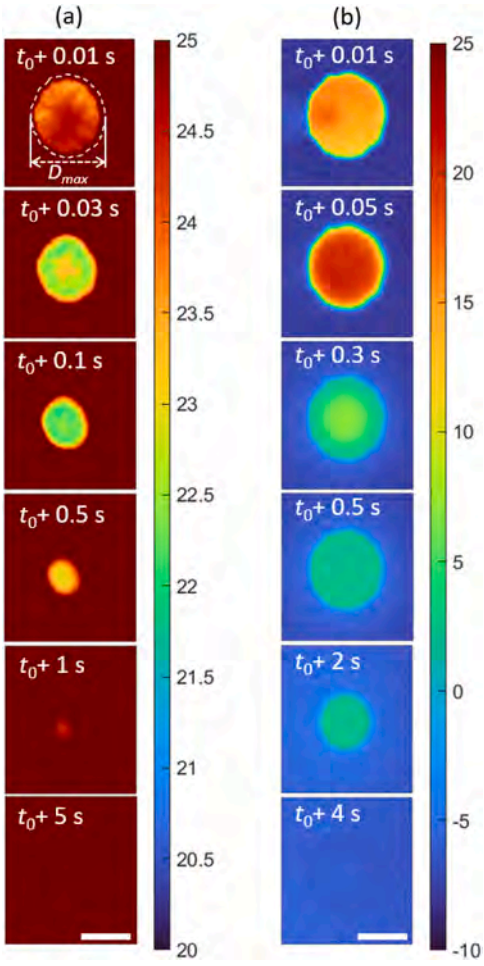

Fig. 10. The time sequence of top view thermal images of droplet impingement on hydrophilic substrates. t_0 indicates the initial time point when the droplet contacted the substrate. (a) $D_d = 2.70$ mm, $V = 1.92$ m/s, $T_s \approx 25$ ℃. (b) $D_d = 2.58$ mm, $V = 1.84$ m/s, $T_s \approx$ -10 ℃. (Scale bar: 5 mm).

which is suggested to be caused by the evaporative cooling effect. Over time, the temperature of the droplet became the same as T_s. After that, a slow evaporation took place in a thermally quasi-steady state.

The thermal evolution of the droplet during the freezing process is shown in Fig. 10(b). After impingement, the temperature at the outer boundary of the droplet rapidly decreased below the freezing temperature. After that, a temperature increase occurred at the center region of the droplet, due to the release of the latent heat of fusion during the solidification phase-change within the droplet. Although the high-speed camera image suggested that the droplet became static in less than 1 second after impingement, the colloidal droplet experienced a much longer thermal process for freezing. In other words, the heat transfer process continued after the droplet formed a static state with a thin disc-like shape on the substrate. Finally, it achieved an equilibrium temperature via heat transfer between the droplet and the substrate.

The experiments of dripping colloidal droplets on substrates with different T_s were repeated three times under each condition to confirm the repeatability. The evolution of D from experiments was represented as D/D_d over time in a linear-log plot, as shown in Fig. 11. The black square and blue cross markers illustrated D/D_d obtained from substrates with $T_s \approx 25$ ℃ and $T_s \approx$ -10 ℃, respectively. $t = 0$ indicated the initial contact time between the droplet and the substrate. The conditions of droplet impingement for each experiment were summarized as follows: When $T_s \approx 25$ ℃, $D_d = 2.54$ mm, 2.56 mm, 2.55 mm, and $V = 1.84$ m/s, 1.85 m/s, 1.84 m/s, respectively. When $T_s \approx$ -10 ℃, $D_d = 2.57$ mm, 2.55 mm, 2.58 mm, and $V = 1.83$ m/s, 1.82 m/s, 1.84 m/s, respectively. *We* and *Re* of droplets were not significantly varied for all experiments, which were averaged as $We = 150$ and $Re = 5330$. Thus, D_{max} was calculated as 8.63 mm as follows based on the averaged $D_d = 2.56$ mm. The red dashed line in Fig. 11 indicates the predicted D_{max}/D_d from this equation. By increasing V and D_d, D_{max} can be increased until *We* of the impinging droplet becomes large enough that the spreading pattern extends beyond the deposition regime [42,64]. Splashing may occur, and the volume of remaining colloidal solution on the substrate will be reduced.

$$S_{max} = \sqrt{\frac{4}{3}Re^{\frac{1}{4}}} = 3.38 \tag{7}$$

$$D_{max} = S_{max}D_d = 8.63 \text{ mm} \tag{8}$$

As shown in Fig. 11, the data of D/D_d with $T_s \approx 25$ ℃ and $T_s \approx$ -10 ℃ agrees well at the beginning of the spreading process. After impingement, D increased rapidly and expanded to its maximum spreading diameter. D_{max} of the droplet at $T_s \approx 25$ ℃ and $T_s \approx$ -10 ℃ were measured as 8.99 mm and 8.75 mm from experimental data, which were

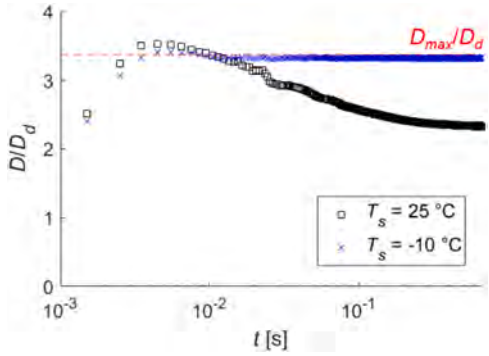

Fig. 11. A linear-log plot of the evolution of droplet diameter after impingement on substrates with different T_s. D was normalized with D_d ($D_d = 2.55 \pm 0.009$ mm and 2.56 ± 0.015 mm for $T_s \approx 25$ ℃ and −10 ℃, respectively). Black square markers and blue cross markers indicate data obtained at $T_s \approx 25$ ℃ and $T_s \approx$ -10 ℃, respectively ($N = 3$). The red dashed line indicates the prediction of D_{max}/D_d from *Re* of droplets.

close to the predicted D_{max}, 8.63 mm. Additionally, D_{max} at $T_s \approx$ -10 ℃ was slightly lower than D_{max} at $T_s \approx$ 25 ℃. The smaller maximum spreading diameter under the freezing condition was consistently observed in the repeated experiments, suggesting that the lower temperature of the droplet indeed has an effect on the spreading dynamics. The rapidly reduced temperature of the droplet due to heat transfer to the precooled substrate caused the viscosity of the droplet to increase. With the same inertia force acting on the droplet, the increase in viscosity inhibited the spreading process and reduced the maximum spreading diameter of the droplet. After the spreading stage, D at $T_s \approx 25$ °C slowly decreased with some fluctuations, which corresponded to the moving contact line oscillation of the droplet during the retraction process. Eventually, D approached a constant value, which allowed interfacial forces along three-phase interfaces to get balanced at the contact line.

The equivalent thickness of the droplet at its maximum spreading diameter (h_d) is considered the characteristic length of the droplet (L), which can be obtained from the volume of the droplet as follows:

$$L = h_d = \frac{\frac{4}{3}\pi\left(\frac{D_d}{2}\right)^3}{\pi\left(\frac{D_{max}}{2}\right)^2} = 0.15 \text{ mm} \tag{9}$$

Bo of the spreading droplets was calculated to be 0.004 based on the range of D_d and L, with air density (ρ_{air}) of 1.20 kg/m^3 at 20 ℃ [65]. This value is smaller than 1, suggesting that gravitational effects on the droplets were minimal. Therefore, studies conducted under these experimental conditions are considered a valid demonstration of small inkjet droplets in the micrometer scale.

Different from the evolution of droplets with $T_s \approx$ 25 ℃, D on a substrate with $T_s \approx$ -10 ℃ arrived at its constant value earlier. The D stopped decreasing after D reached D_{max}. Based on the same L obtained from the cylindrical shape approximation of the spreading droplet, h of water under natural convection condition (= 200 ~ 1000 W/m^2·K) [66], and k of saturated water at around 22 ℃ (= 0.606 W/m·K) [67], *Bi* was calculated to be 0.05 ~ 0.25. The value was not always smaller than 0.1, which suggests that only part of a droplet can have a transient freezing process in this study, compared to micrometer-scale droplets that have an order of magnitude smaller L. According to high-speed images and thermal images of the droplet during freezing, it was validated that the droplet was not completely frozen at its maximum spreading diameter. While the oscillation continued, no significant change was shown in the evolution of D. The frozen thin layer at the bottom of the droplet prevented the receding of the contact line. As a result, the final D when the droplet completely froze on the substrate with $T_s \approx$ -10 ℃ appeared very close to D_{max}. This remains valid when the same substrates were used. Surface properties of the substrate can influence D_{max} and the spreading process of the droplets. It is worth mentioning that, the smaller droplet, *i.e.*, micrometer scale, in practical 3D printing applications would promote a faster freezing process, which can create even finer printing resolution and more uniform particle distributions.

4.2. B. Evolution of frozen colloidal droplets during sublimation

The heat transfer between the droplet and the substrate during the droplet freezing process is equal to the sum of the latent heat of solidification of the droplet and the heat released by the cooling substrate. The freezing time of the droplet ($t_{freezing}$) can be predicted as follows [68]:

$$t_{freezing} = \frac{R_T m h_d [H_{sl} + c(T_d - T_F)]}{\pi\left(\frac{D_{max}}{2}\right)^2 (T_F - T_s)} = 1.61 \text{ s} \tag{10}$$

Here, R_T is the thermal resistance of water (= $1/k$ = 1.63 mK/W at 25 ℃) [67], m is the mass of droplet (= $\frac{4}{3}\pi\left(\frac{D_d}{2}\right)^3\rho$ = 8.78 × 10^{-6} kg), H_{sl} is the latent heat of ice (= 3.34 × 10^5 J/kg) [69], c is the specific heat capacity of water (= 4179 J/kg·K at 25 ℃) [67], T_d is the temperature of droplet (= 25 ℃), and T_F is the freezing temperature of droplet (= 0 ℃). In this study, $t_{freezing}$ was longer than the time duration of the droplet dynamic process shown in Fig. 11. It is expected that $t_{freezing}$ can be significantly reduced when the size of droplets becomes smaller.

After droplets were frozen on substrates, a sublimation-based drying process was performed. The geometrical evolution of the frozen droplets was recorded using a monochrome digital camera. The time sequence of side view images of different frozen droplets was summarized in Fig. 12: a droplet of distilled water impinged on the surface with $T_s \approx$ 25 ℃ before freeze-drying (sublimation), a colloidal droplet impinged on the surface with $T_s \approx$ 25 ℃ before freeze-drying, and a colloidal droplet impinged and froze on the surface with $T_s \approx$ -10 ℃ before freezing-drying, respectively. For these three cases, the impinging conditions were similar. D_d was 2.59 ± 0.009 mm, and V was 1.85 ± 0.004 m/s, respectively. The sublimation process was operated via freezing, vacuum freezing, and heating functions of the freeze dryer. t_0 was determined as the beginning of the sublimation process when the pressure of the freeze dryer became lower than the pressure at the triple point on the phase change diagram of water.

Fig. 12(a) illustrates the sublimation process of a distilled water droplet in the freeze dryer. It should be noted that the liquid droplet in this case first experienced a freezing process in the freeze dryer, followed by sublimation. It is seen that the frozen water molecules shift to water vapor along the surface of the frozen droplet layer-by-layer. As time went on, the angle between the frozen droplet and the substrate surface was also increased gradually. During the sublimation process, both the frozen droplet's diameter and height decreased, a so-called self-similar process. In the end, the frozen droplet was dried completely from the substrate.

For the colloidal droplets, however, no significant shape change of the frozen droplet was observed during sublimation, as shown in Fig. 12 (b) and (c). This indicates that sublimated water vapor would not bring colloidal particles into the air from the droplet. Instead, the intensity contrast of the droplet area decreased over time, suggesting a less solid composition within the droplet, *i.e.*, the formation of a porous structure on the substrate. The intensity contrast decreased because illumination light could pass through this porous structure, which made the object brighter. These porous structures formed by colloidal particles were fragile. After the sublimation process, colloidal particles collapsed onto the surface of the substrate, forming the deposition patterns. Notably, the colloidal droplets that impinged and froze on the substrate prior to freeze drying—resulting in disc-like frozen droplets—exhibited a larger surface area, leading to the shortest sublimation times observed in this study.

The sublimation process of frozen droplets on substrates was investigated in repeated experiments. The evolutions of D and H for different droplets during the sublimation process were represented in linear-linear plots shown in Fig. 13(a) and (b), respectively. Green markers show the reference data obtained from the distilled water droplet (D_d = 2.60 mm) case. The droplet was dripped on a substrate with $T_s \approx$ 25 °C and was frozen in the freeze dryer after it achieved a static state. Black and blue markers indicate the averaged data obtained from colloidal droplets on substrates with $T_s \approx$ 25 ℃ and $T_s \approx$ -10 ℃ in repeated experiments for each case. The sizes of droplets were D_d = 2.62 ± 0.035 mm, and D_d = 2.59 ± 0.006 mm, respectively. For $T_s \approx$ 25 ℃ cases, droplets were frozen in the freeze dryer after becoming static, so the shape of the frozen droplet was a spherical cap, the same as the frozen distilled water droplet. For $T_s \approx$ -10 ℃ cases, droplets were frozen upon impinging on the precooled substrates. As mentioned previously, the shape of frozen droplets was a disc-like shape. After measuring D and H from captured images, they were normalized with D_d. t = 0 indicated

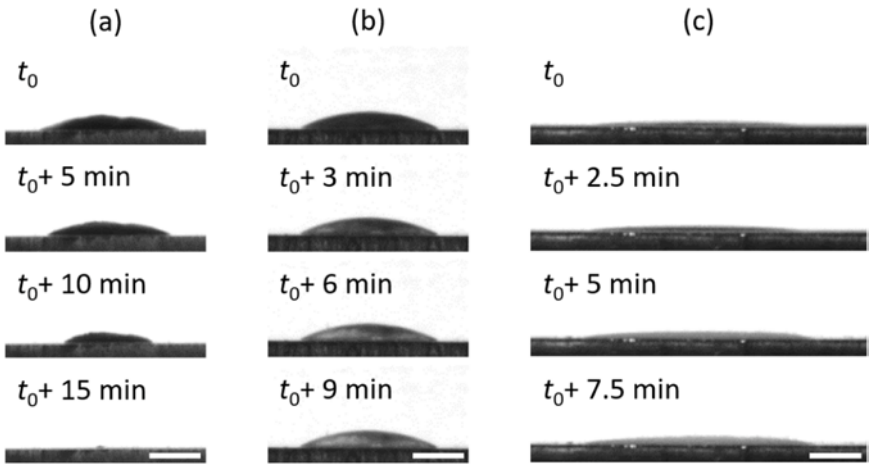

Fig. 12. The time sequences of side view images of droplets during the sublimation process. t_0 indicates the beginning of sublimation. (a) Distilled water droplet impinged on the surface with $T_s \approx 25$ °C before freeze-drying (sublimation), $D_d = 2.60$ mm, $V = 1.85$ m/s. (b) Colloidal droplet impinged on the surface with $T_s \approx 25$ °C before freeze-drying, $D_d = 2.58$ mm, $V = 1.85$ m/s. (c) Colloidal droplet impinged and froze on the surface with $T_s \approx$ -10 °C before freezing-drying, $D_d = 2.59$ mm, $V = 1.86$ m/s. (Scale bar: 2 mm).

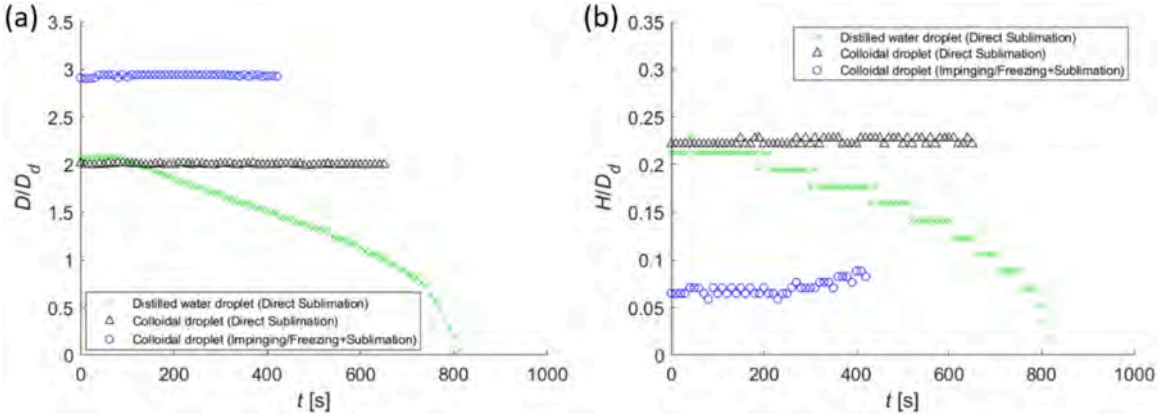

Fig. 13. A linear-linear plot of the geometrical evolutions of droplets during sublimation. (a) The normalized diameter of droplets (D/D_d) over time (t). (b) The normalized height of droplets (H/D_d) over time (t). $t = 0$ indicates the beginning of the sublimation when the chamber pressure became lower than the pressure at the triple point of water. Green cross markers indicate data obtained using distilled water droplet through direct sublimation ($N = 1$). Black triangle markers indicate data obtained using colloidal droplet through direct sublimation only ($N = 3$). Blue circle markers indicate data obtained using colloidal droplet through impinging/freezing followed by sublimation ($N = 3$).

the beginning of the sublimation process, which was determined when the pressure of the sublimation chamber decreased to below the triple point of water (= 611.66 Pa) in the phase change diagram [61]. In this study, the experiment using distilled water was operated one time as a reference, and experiments using colloidal droplets were repeated three times for each condition.

As shown in Fig. 13, D/D_d and H/D_d of the distilled water droplet decreased concurrently during the sublimation process. For colloidal droplets, however, D/D_d and H/D_d were almost constant during the entire sublimation processes. Since the colloidal particles were not removed from the droplet along with the escaping water vapor during the sublimation process, and no fluidic motion existed that could relocate colloidal particles, the boundary profiles of frozen colloidal droplets were not changed significantly over time in these plots.

Interestingly, H/D_d showed more fluctuations as well as an increasing trend over time from experiments using the disc-like shaped colloidal droplet (which was formed through impinging and freezing processes). It is suggested that along with the sublimation process of water from the frozen disc-like colloidal droplets, fluffy and porous structures were formed by colloidal particles and were loose from the surface of the substrate, which altered the height profiles as shown in Fig. 13(b).

4.3. C. Deposition patterns formed through freezing and sublimation

After the drying processes (through evaporation or sublimation) were completed, the colloidal particles were deposited on the surface, and the images of the deposition patterns were captured to evaluate the printing quality. Fig. 14 shows sample images of the deposition patterns formed through different drying approaches: (a) Deposition of colloidal droplet through impinging and evaporation at $T_s \approx 25$ ℃; (b) Deposition of colloidal droplet through impinging on the surface of $T_s \approx 25$ ℃, followed by sublimation in freeze dryer (with the formation of spherical-shaped droplet); (c) Deposition of colloidal droplet through impinging and freezing on surface of $T_s \approx$ -10 ℃, followed by sublimation (with the formation of disclike droplet). The impingement conditions of droplets shown in Fig. 14(a), (b), and (c) were $D_d = 2.54$ mm, 2.57 mm, and 2.59 mm, respectively.

The left column images in Fig. 14 show the deposition patterns of colloidal droplets through the different drying approaches. It is clearly seen that the deposition processes without impinging and freezing (cases (a) and (b)) produced similar deposition areas on substrates as shown in

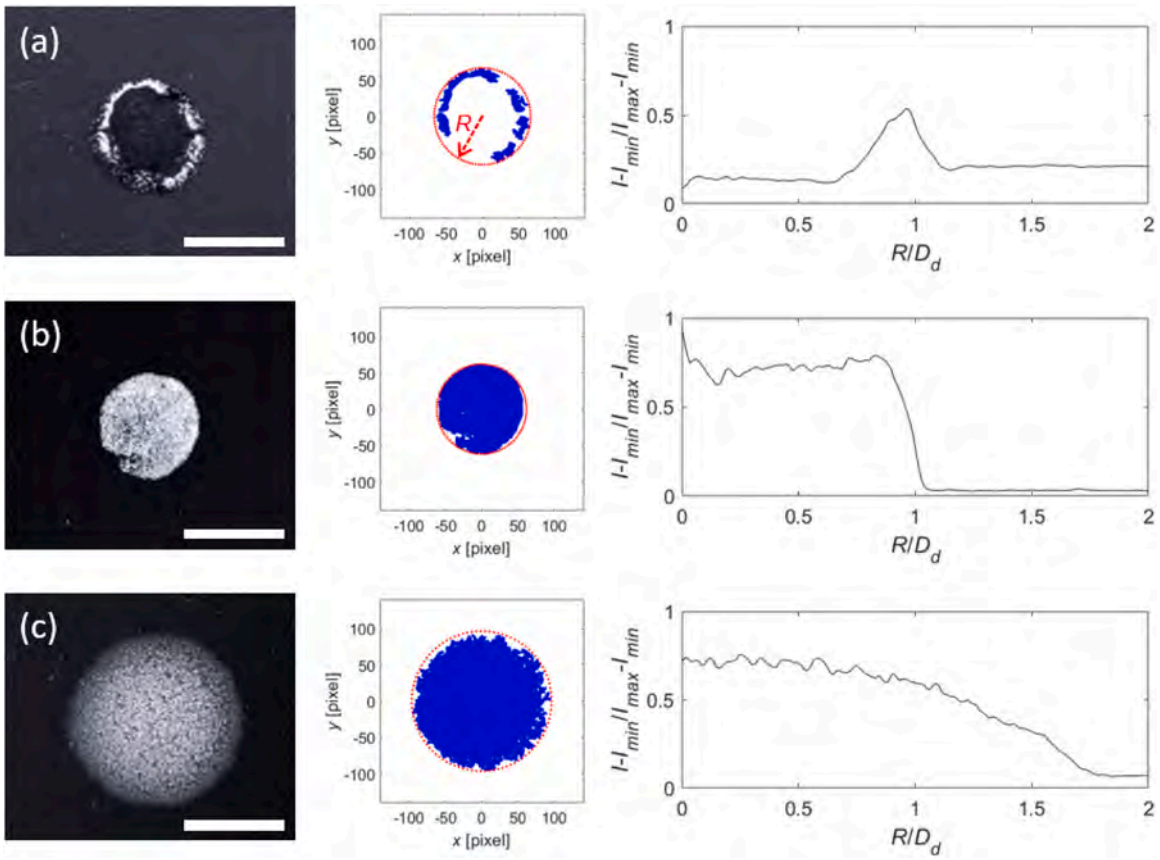

Fig. 14. Sample deposition patterns of colloidal droplets formed through different drying approaches: (a) deposition through impinging and evaporation at $T_s \approx 25$ ℃. $D_d = 2.54$ mm. (b) deposition through impinging on the surface of $T_s \approx 25$ ℃, followed by sublimation in freeze dryer (with the formation of spherical-shaped droplet). $D_d = 2.57$ mm. (c) deposition through impinging/freezing on surface of $T_s \approx$ -10 ℃, followed by sublimation (with the formation of disc-like droplet). $D_d = 2.59$ mm. The top-view images of the colloidal deposition patterns, the diagrams of the printing area of colloidal particles, and the plots of the intensity profiles were illustrated in the left, middle, and right columns, respectively. (Scale bar: 5 mm).

Fig. 14(a) and (b). It is because the colloidal droplets under these conditions reached static state as liquid with the same final contact areas and contact angles before the drying processes. Though the drying methods are different, the deposition footprint areas appear very similar. In contrast, the deposition area produced through impinging, freezing, and sublimation (case (c)) appears larger, as shown in Fig. 14 (c). This is due to the "locking effect" when the colloidal droplet froze during the impinging and spreading process. It should be noted that, while a larger deposition area was produced in this particular case of colloidal droplet impinging and freezing on the surface of $T_s \approx$ -10 ℃, followed by sublimation, a wide range of deposition areas are expected to be generated by controlling the droplet impingement process and environmental conditions, influencing both the freezing rates and impact dynamics. For example, instant freezing of a colloidal droplet upon impacting (minimized spreading) would generate a much smaller deposition area. It can be achieved by decreasing T_s, reducing D_d, or lowering the temperature of the droplets. In our preliminary studies, a rapid freezing process was observed when the droplet was supercooled before impingement on precooled substrate surfaces.

While different drying methods influence the deposition area, the distribution of colloidal particles — and thus the deposition patterns — are more significantly impacted by the drying methods. Fig. 14(a) shows the deposition pattern formed through the conventional evaporation-based drying method. Due to the Deegan flow within the liquid colloidal droplet during evaporation, the particles suspended in the droplet were brought toward the edge of the contact line of the droplet, which caused a high concentration region of deposition in a coffee ring-like pattern. In contrast, colloidal particles in Fig. 14(b) and (c) were distributed more uniformly over the entire deposition area. It is suggested that the particles were kept in place with minimum redistribution during the sublimation process. As a result, these particles could settle down to the surface to form patterns with much more uniform deposit distributions than evaporation-based drying cases. It is also found that the density of particles in the printed area was lower in Fig. 14(c) than in Fig. 14(b). With the same amount of the particles suspended in the droplet, a larger deposition area would produce a less dense deposit distribution. However, it should be noted that since the deposition area can be controlled in the freezing-based method, the deposit density could also be modulated by controlling the freezing rate and impacting dynamics of colloidal droplet during printing.

Colloidal particles in the droplet were flowed with the deformation of the droplets during the impingement and spreading process [70]. Different liquids may need to be selected as solvents for particles of varying sizes or densities to ensure that the particles remain suspended in the droplets and follow fluidic motion during 3D printing. To prevent the particles' motion from being dominated by inertia along their initial trajectory, the Stokes number (St) of the colloidal particles in the droplets of the selected solvent should be small. Here, St represents the ratio of the particle relaxation time to the characteristic time scale of fluid. In this study, St of particles was solved as follows, where ρ_p and D_p indicate the density and diameter of colloidal particles, respectively [71]. Averaged values of V (= 1.84 m/s) and D_d (= 2.56 mm) were used.

$$St = \frac{(\rho_p - 0.5\rho)(D_p)^2 V}{18\mu D_d} = 0.91 \quad (11)$$

$St < 1$ suggests that colloidal particles within the droplet will follow

the fluid motion during the spreading and receding processes after impingement on the substrate. According to experimental and simulation studies using similar particle properties, concentrations, and impingement conditions, a one-way coupling between the liquid phase and particles was confirmed during droplet impingement. As the droplet spreads, colloidal particles are carried radially along the direction of the propagating rim and are then pulled back during the receding process, with no particles leaving the droplet.

One exception may occur during the receding motion. It was found that only a few particles were carried upwards at the center of the droplet when the receding droplet reached its maximum height. This created a dry spot with a limited number of particles in the droplet, but particles could return to this center region when the dry spot was refilled with liquid again during the oscillatory motion. After the droplet reached equilibrium, it was found that the effects of impingement on the distribution of particles in the droplet were limited [71].

This is also validated by the observation from Fig. 14, where the particle distribution in the deposition pattern only changed with variations in the droplet thickness gradient on the substrates. After impingement, the droplet reached a steady state within 25 ms, which was shorter than $t_{freezing}$. This suggests that the droplet was frozen in an equilibrium state with uniform particle distributions in the liquid. This led to the conclusion that the distribution of particles experienced limited effects from the fluidic motions of the droplet during impingement.

To quantify the deposition densities formed through the different methods, the deposition patterns in the left column were digitized, as shown in the middle column in Fig. 14. In these graphs, the x- and y-axis indicate the pixel coordinates, respectively. The blue dots indicate pixels covered by colloidal particles on substrates, and the red dotted lines indicate the deposition areas on substrates. The coverage area ratio (AR) is defined as the ratio between the number of pixels of colloidal particles (N_p) and the total pixels of the deposition area (N_d) on substrates, i.e., $AR = N_p/N_d \times 100$ %. In this study, multiple trials were conducted for each case. Detailed results of the repeated measurements were illustrated in Table 1. The average AR of the obtained deposition patterns from the evaporation-based drying method is 12.01 ± 2.16 %, which is mainly contributed by the deposits along the edge of the deposition region. On the other hand, the average ARs of the patterns obtained from the sublimation-based drying method are 85.50 ± 8.32 % (direct sublimation) and 85.12 ± 6.14 % (impinging/freezing + sublimation), respectively. It suggested that the sublimation-based drying method could provide much more uniform and dense colloidal deposition.

Efforts were also made to extract the intensity profiles of the deposition patterns, as shown in the right column in Fig. 14. The x-axis is R/D_d, the normalized distance from the center of the droplet along the radial direction. The y-axis is the scaled I from images using I_{max} and I_{min}. For the intensity profile shown in Fig. 14(a), the peak I was found near $R/D_d = 1$, corresponding to the droplet's contact line. It implied that colloidal particles in the droplet were gathered along the contact line of the droplet with high concentration. In addition, I in the center was almost zero, indicating a void in the center of the deposition area. For the intensity profile shown in Fig. 14(b), colloidal particles were distributed uniformly in the deposition area, $0 < R/D_d < 1$. At $R/D_d > 1$, a clear step on I was observed, indicating a sharp boundary of the printed pattern. It should be mentioned that the colloidal particles were distributed in a three-dimensional shape after the sublimation process. However, the deposition pattern and the subsequent analysis were obtained based on the two-dimensional projection top-view of the deposits, which consisted of multiple layers stacked together within the deposition area. All printed patterns in this study were obtained from similarly sized droplets. A larger thickness of the deposition patterns resulted when the deposition area of the droplets on the substrates was small. As a result, even though the inkjet solution droplets on the substrates were spherical, the concentration of particles at the edge and at the center of the deposition area on the substrate could not be clearly distinguished if both of them were high. Thus, when the deposition area was small (particle density was high), the captured deposition pattern would not be able to display the thickness variations of the deposits, but only a uniform circular pattern with a sharp boundary. For the intensity profile shown in Fig. 14(c), the colloidal particles were also distributed uniformly. However, a smooth decreasing trend of I was observed from $R/D_d = 0$ to $R/D_d = 1.8$, from the center to the boundary of the droplet. The slight change in I over R was measurable because the density of particles was lower when the deposition area became larger. Though the colloidal particles were also stacked in three-dimensional after the sublimation process, the inter-particle spacings would become larger. At the outer area, the deposition thickness appeared smaller with less particles, thus displaying a lower intensity in the extracted intensity profile. This suggested that the freezing-sublimation-based method could essentially "lock" the colloidal particles in place, and produce a more uniform deposit distribution. In the meantime, a three-dimensional deposition pattern could form, in which the density of deposition particles correlates to the local thickness of the colloidal droplet.

5. Conclusions

In this study, a novel freezing-sublimation-based method was developed to fundamentally improve the quality of inkjet-based 3D printing technology. To overcome the non-uniform distribution of deposition patterns of individual ink drops, colloidal droplets are frozen rapidly upon impinging on substrates, followed by a sublimation process to remove the solvent. These processes are demonstrated to prevent the undesired transport and redistribution of the colloidal particles suspended in the droplet. Thus, the final deposits can form a printing pattern with uniform distributions.

In the process of colloidal droplet impinging on substrates, with well-controlled impact conditions, the spreading diameter of droplets on substrates can be predicted. When T_s is below the freezing point, the final shape of droplets varies, depending on the competing outcome of the heat transfer process (freezing rate) and the hydrodynamics during impinging. In this paper, as a proof of concept, detailed observations and analysis were conducted focusing on room-temperature colloidal droplet impinging on a substrate with T_s = -10 ℃. It is found that the colloidal droplet freezes during the spreading process upon impacting, forming a disc-like ice drop on the surface.

During the sublimation process, the frozen water becomes vapor directly, escaping from the colloidal drop, while the colloidal particles remain in place, forming a three-dimensional structure on the substrate. These deposits then form printed patterns on substrates. A slight decrease in deposit density may present along the radial direction of the droplet, corresponding to the reduction of the height from the center to

Table 1
The coverage area ratios of colloidal particles on substrates under different drying methods with different shaped droplets ($N = 3$).

Drying Method	Evaporation			Sublimation					
Shape	Spherical Droplet			Spherical Droplet			Disc-like Droplet		
N_p	1997	1457	1953	10356	10187	9802	22778	23608	26492
N_d	13777	13608	18067	11974	13279	10508	29189	26760	29736
AR (%)	14.50	10.71	10.81	86.49	76.72	93.28	78.04	88.22	89.09
AR_{avg} (%)	12.01 ± 2.16			85.50 ± 8.32			85.12 ± 6.14		

the boundary of the frozen droplet on substrates. Since there is no internal flows that can redistribute the particles, the final deposition patterns appear much more uniform in comparison to those formed in the conventional evaporation-based drying processes. Additionally, the deposition coverage area ratio is found to increase to about 90 % compared to the 10 % provided by the evaporation-based drying method.

In conclusion, the novel freezing-sublimation-based method is demonstrated to be capable of producing much more uniform deposition patterns of each ink drop in inkjet-based 3D printing processes, thus fundamentally improving the printing quality. This work will serve as the technical and theoretical basis for the development and validation of the novel freezing-based inkjet 3D printing technique for fabricating high-quality functional structures.

CRediT authorship contribution statement

Zhang Haipeng: Writing – original draft, Visualization, Methodology, Formal analysis, Data curation. **Zhang Xiaoxiao:** Methodology, Formal analysis, Data curation. **Liu Yang:** Writing – review & editing, Validation, Supervision, Software, Resources, Project administration, Methodology, Investigation, Funding acquisition, Formal analysis, Conceptualization.

Declaration of Competing Interest

The authors declare that they have no known competing financial interests or personal relationships that could have appeared to influence the work reported in this paper.

Acknowledgments

The research work is supported by the National Science Foundation (NSF), under Award Number: 2242311.

Data availability

Data will be made available on request.

References

[1] Y. Guo, H.S. Patanwala, B. Bognet, Inkjet and inkjet-based 3D printing: connecting fluid properties and printing performance, Rapid Prototyp. J. 23 (2017) 562–576.
[2] T.D. Ngo, A. Kashani, G. Imbalzano, K.T.Q. Nguyen, D. Hui, Additive manufacturing (3D printing): a review of materials, methods, applications and challenges, Compos B Eng. 143 (2018) 172–196.
[3] N. Shahrubudin, T.C. Lee, R.J.P.M. Ramlan, An overview on 3D printing technology: technological, materials, and applications, Procedia Manuf. 35 (2019) 1286–1296.
[4] Q. Yan, H. Dong, J. Su, J. Han, B. Song, Q. Wei, Y. Shi, A review of 3D printing technology for medical applications, Engineering 4 (2018) 729–742.
[5] H. Yoo, C. Kim, Experimental studies on formation, spreading and drying of inkjet drop of colloidal suspensions, Colloids Surf. A Physicochem Eng. Asp. 468 (2015) 234–245.
[6] B. Derby, Inkjet printing of functional and structural materials: fluid property requirements, feature stability, and resolution, Annu Rev. Mater. Res 40 (2010) 395–414, https://doi.org/10.1146/annurev-matsci-070909-104502.
[7] I.M. Hutchings, G.D. Martin, Introduction to Inkjet Printing for Manufacturing, in: Inkjet Technology for Digital Fabrication, John Wiley and Sons, Ltd, 2012, pp. 1–20, https://doi.org/10.1002/9781118452943.ch1.
[8] J.R. Castrejon-Pita, W.R.S. Baxter, J. Morgan, S. Temple, G.D. Martin, I. M. Hutchings, Future, opportunities and challenges of inkjet technologies, At. Sprays 23 (2013) 541–565.
[9] A.L. Yarin, Drop impact dynamics: splashing, spreading, receding, bouncing…, Annu Rev. Fluid Mech. 38 (2006) 159–192.
[10] H.-Y. Kim, J.-H. Chun, The recoiling of liquid droplets upon collision with solid surfaces, Phys. Fluids 13 (2001) 643–659, https://doi.org/10.1063/1.1344183.
[11] Y. Liu, Z. Zhang, H. Hu, H. Hu, A. Samanta, Q. Wang, H. Ding, An experimental study to characterize a surface treated with a novel laser surface texturing technique: water repellency and reduced ice adhesion, Surf. Coat. Technol. 374 (2019) 634–644, https://doi.org/10.1016/j.surfcoat.2019.06.046.
[12] S. Mandre, M.P. Brenner, The mechanism of a splash on a dry solid surface, J. Fluid Mech. 690 (2012) 148–172, https://doi.org/10.1017/jfm.2011.415.
[13] R.D. Deegan, O. Bakajin, T.F. Dupont, G. Huber, S.R. Nagel, T.A. Witten, Capillary flow as the cause of ring stains from dried liquid drops, Nature 389 (1997) 827–829.
[14] H. Hu, R.G. Larson, Analysis of the effects of Marangoni stresses on the microflow in an evaporating sessile droplet, Langmuir 21 (2005) 3972–3980.
[15] H. Wijshoff, Drop dynamics in the inkjet printing process, Curr. Opin. Colloid Interface Sci. 36 (2018) 20–27, https://doi.org/10.1016/j.cocis.2017.11.004.
[16] R.D. Deegan, O. Bakajin, T.F. Dupont, G. Huber, S.R. Nagel, T.A. Witten, Contact line deposits in an evaporating drop, Phys. Rev. E 62 (2000) 756–765, https://doi.org/10.1103/PhysRevE.62.756.
[17] K.N. Al-Milaji, H. Zhao, Probing the colloidal particle dynamics in drying sessile droplets, Langmuir 35 (2019) 2209–2220.
[18] M. Pack, H. Hu, D.O. Kim, X. Yang, Y. Sun, Colloidal drop deposition on porous substrates: competition among particle motion, evaporation, and infiltration, Langmuir 31 (2015) 7953–7961, https://doi.org/10.1021/acs.langmuir.5b01846.
[19] J. Sun, B. Bao, M. He, H. Zhou, Y. Song, Recent advances in controlling the depositing morphologies of inkjet droplets, ACS Appl. Mater. Interfaces 7 (2015) 28086–28099, https://doi.org/10.1021/acsami.5b07006.
[20] M. Anyfantakis, D. Baigl, Dynamic photocontrol of the coffee-ring effect with optically tunable particle stickiness, Angew. Chem. Int. Ed. 53 (2014) 14077–14081, https://doi.org/10.1002/anie.201406903.
[21] W.D. Ristenpart, P.G. Kim, C. Domingues, J. Wan, H.A. Stone, Influence of substrate conductivity on circulation reversal in evaporating drops, Phys. Rev. Lett. 99 (2007) 234502, https://doi.org/10.1103/PhysRevLett.99.234502.
[22] D.O. Kim, A. Rokoni, P. Kaneelil, C. Cui, L.H. Han, Y. Sun, Role of surfactant in evaporation and deposition of bisolvent biopolymer droplets, Langmuir 35 (2019) 12773–12781, https://doi.org/10.1021/acs.langmuir.9b01705.
[23] P.Q.M. Nguyen, L.-P. Yeo, B.-K. Lok, Y.-C. Lam, Patterned surface with controllable wettability for inkjet printing of flexible printed electronics, ACS Appl. Mater. Interfaces 6 (2014) 4011–4016, https://doi.org/10.1021/am4054546.
[24] D.-O. Kim, M. Pack, H. Hu, H. Kim, Y. Sun, Deposition of colloidal drops containing ellipsoidal particles: competition between capillary and hydrodynamic forces, Langmuir 32 (2016) 11899–11906.
[25] V.H. Chhasatia, Y. Sun, Interaction of bi-dispersed particles with contact line in an evaporating colloidal drop, Soft Matter 7 (2011) 10135–10143, https://doi.org/10.1039/C1SM06393F.
[26] V.H. Chhasatia, A.S. Joshi, Y. Sun, Effect of relative humidity on contact angle and particle deposition morphology of an evaporating colloidal drop, Appl. Phys. Lett. 97 (2010) 231909, https://doi.org/10.1063/1.3525167.
[27] E. Sowade, T. Blaudeck, R.R. Baumann, Self-assembly of spherical colloidal photonic crystals inside inkjet-printed droplets, Cryst. Growth Des. 16 (2016) 1017–1026.
[28] K.N. Al-Milaji, V. Radhakrishnan, P. Kamerkar, H. Zhao, pH-modulated self-assembly of colloidal nanoparticles in a dual-droplet inkjet printing process, J. Colloid Interface Sci. 529 (2018) 234–242.
[29] H. Lian, L. Qi, J. Luo, K. Hu, Uniform nitrogen-doped graphene lines with favorable outlines printed by elaborate regulation of drying and overlapping, Appl. Surf. Sci. 473 (2019) 614–621.
[30] J. Niu, L. Qi, H. Lian, J. Luo, R. Zhang, X. Chao, Revisiting the inhomogeneity in drop-on-demand printing of graphene: an effective route for overcoming the coffee-ring effect, Surf. Interfaces 46 (2024) 104036.
[31] R. Dash, Y. Li, A.J. Ragauskas, Cellulose nanowhisker foams by freeze casting, Carbohydr. Polym. 88 (2012) 789–792.
[32] S. Deville, Freeze-casting of porous ceramics: a review of current achievements and issues, Adv. Eng. Mater. 10 (2008) 155–169.
[33] A. Gannarapu, B.A. Gozen, Freeze-Printing of liquid metal alloys for manufacturing of 3D, conductive, and flexible networks, Adv. Mater. Technol. 1 (2016) 1600047.
[34] Z. Wang, S.J. Florczyk, Freeze-FRESH: a 3D printing technique to produce biomaterial scaffolds with hierarchical porosity, Materials 13 (2020) 354.
[35] A. Elkaseer, S. Schneider, Y. Deng, S.G. Scholz, Effect of process parameters on the performance of drop-on-demand 3D inkjet printing: geometrical-based modeling and experimental validation, Polymers 14 (2022) 2557.
[36] Y.K. Kim, J.A. Park, W.H. Yoon, J. Kim, S. Jung, Drop-on-demand inkjet-based cell printing with 30-μm nozzle diameter for cell-level accuracy, Biomicrofluidics 10 (2016).
[37] R. Rioboo, C. Tropea, M. Marengo, Outcomes from a drop impact on solid surfaces, At. Sprays 11 (2001).
[38] R. Bhardwaj, X. Fang, D. Attinger, Pattern formation during the evaporation of a colloidal nanoliter drop: a numerical and experimental study, N. J. Phys. 11 (2009) 075020.
[39] E. Sowade, T. Blaudeck, R.R. Baumann, Self-assembly of spherical colloidal photonic crystals inside inkjet-printed droplets, Cryst. Growth Des. 16 (2016) 1017–1026.
[40] H. Yoo, C. Kim, Experimental studies on formation, spreading and drying of inkjet drop of colloidal suspensions, Colloids Surf. A Physicochem Eng. Asp. 468 (2015) 234–245.
[41] P.G. Bange, N.D. Patil, R. Bhardwaj, Impact dynamics of a droplet on a heated surface, in: Proceedings of the 5th International Conference of Fluid Flow, Heat and Mass Transfer (FFHMT '18), Niagara Falls, ON, Canada, 2018: pp. 7–9.
[42] S. Moghtadernejad, C. Lee, M. Jadidi, An introduction of droplet impact dynamics to engineering students, Fluids 5 (2020) 107.
[43] A.L. Yarin, Drop impact dynamics: splashing, spreading, receding, bouncing…, Annu. Rev. Fluid Mech. 38 (2006) 159–192.
[44] P. Zhao, G.K. Hargrave, H.K. Versteeg, C.P. Garner, B.A. Reid, E.J. Long, H. Zhao, The dynamics of droplet impact on a heated porous surface, Chem. Eng. Sci. 190 (2018) 232–247.

[45] H. Jones, Cooling, freezing and substrate impact of droplets formed by rotary atomization, J. Phys. D. Appl. Phys. 4 (1971) 1657.
[46] R. Zhang, P. Hao, X. Zhang, F. He, Supercooled water droplet impact on superhydrophobic surfaces with various roughness and temperature, Int J. Heat. Mass Transf. 122 (2018) 395–402.
[47] K.C. Patel, X.D. Chen, Surface-center temperature differences within milk droplets during convective drying and drying-based Biot number analysis, AIChE J. 54 (2008) 3273–3290.
[48] Y. Wang, F. Liu, Y. Yang, L.-P. Xu, Droplet evaporation-induced analyte concentration toward sensitive biosensing, Mater. Chem. Front 5 (2021) 5639–5652.
[49] R. Mollaret, K. Sefiane, J.R.E. Christy, D. Veyret, Experimental and numerical investigation of the evaporation into air of a drop on a heated surface, Chem. Eng. Res. Des. 82 (2004) 471–480.
[50] G. McHale, S. Aqil, N.J. Shirtcliffe, M.I. Newton, H.Y. Erbil, Analysis of droplet evaporation on a superhydrophobic surface, Langmuir 21 (2005) 11053–11060.
[51] H. Hu, R.G. Larson, Evaporation of a sessile droplet on a substrate, J. Phys. Chem. B 106 (2002) 1334–1344.
[52] Y.O. Popov, Evaporative deposition patterns: spatial dimensions of the deposit, Phys. Rev. E Stat. Nonlinear Soft Matter Phys. 71 (2005) 036313.
[53] R.D. Deegan, O. Bakajin, T.F. Dupont, G. Huber, S.R. Nagel, T.A. Witten, Capillary flow as the cause of ring stains from dried liquid drops, Nature 389 (1997) 827–829.
[54] A.T. Tyowua, A.I. Ezekwuaku, Overcoming coffee-stain effect by particle suspension marble evaporation, Colloids Surf. A Physicochem Eng. Asp. 629 (2021) 127386.
[55] S. Wang, A.A. Darhuber, A numerical model for the transport and drying of solutions in thin porous media—coffee-stain effect and solute ring formation, Colloids Surf. A Physicochem Eng. Asp. 682 (2024) 132839.
[56] E. Jambon-Puillet, N. Shahidzadeh, D. Bonn, Singular sublimation of ice and snow crystals, Nat. Commun. 9 (2018) 4191.
[57] J. Nelson, Sublimation of ice crystals, J. Atmos. Sci. 55 (1998) 910–919.
[58] H.-Y. Tung, Z.-Y. Guan, T.-Y. Liu, H.-Y. Chen, Vapor sublimation and deposition to build porous particles and composites, Nat. Commun. 9 (2018) 2564.
[59] F.K. Hansen, G. Rødsrud, Surface tension by pendant drop: I. A fast standard instrument using computer image analysis, J. Colloid Interface Sci. 141 (1991) 1–9.
[60] M.-W. Yang, S.-Y. Lin, A method for correcting the contact angle from the θ/2 method, Colloids Surf. A Physicochem Eng. Asp. 220 (2003) 199–210.
[61] H. Mao, Z. Qiu, B. Xie, Z. Wang, Z. Shen, W. Hou, Development and application of ultra-high temperature drilling fluids in offshore oilfield around Bohai Sea bay basin, China, in: Offshore Technology Conference Asia, OTC, 2016 p. D042S006R019.
[62] F. Wang, L. Yang, L. Wang, Y. Zhu, T. Fang, Maximum spread of droplet impacting onto solid surfaces with different wettabilities: adopting a rim–lamella shape, Langmuir 35 (2019) 3204–3214.
[63] Y. Yonemoto, K. Tashiro, K. Shimizu, T. Kunugi, Predicting the splash of a droplet impinging on solid substrates, Sci. Rep. 12 (2022) 5093.
[64] A.V. Mahulkar, G.B. Marin, G.J. Heynderickx, Droplet–wall interaction upon impingement of heavy hydrocarbon droplets on a heated wall, Chem. Eng. Sci. 130 (2015) 275–289.
[65] F.M. White, H. Xue, Fluid mechanics, McGraw-hill, New York, 2003.
[66] M. Xiao, L. Tang, X. Zhang, I.Y.F. Lun, Y. Yuan, A review on recent development of cooling technologies for concentrated photovoltaics (CPV) systems, Energies 11 (2018) 3416.
[67] T.L. Bergman, Fundamentals of heat and mass transfer, John Wiley & Sons, 2011.
[68] X. Wang, B. Xu, S. Guo, Y. Zhao, Z. Chen, Droplet impacting dynamics: recent progress and future aspects, Adv. Colloid Interface Sci. 317 (2023) 102919.
[69] W. Kang, M. Jansen, On icy ocean worlds, size controls ice shell geometry, Astrophys J. 935 (2022) 103.
[70] B.S. Lekshmi, A.P. Joseph, S.N. Varanakkottu, Exploiting droplet impact-driven flows and jetting to guide and extract particles from particle-laden droplets, Phys. Fluids 36 (2024).
[71] R. Tribess, K. Nabbout, M. Sommerfeld, Particle-laden droplets impinging a wall at low particle concentrations, in: ILASS Europe 2023, 32 Nd European Conference on Liquid Atomization & Spray Systems, Napoli, Italy, 2023.